MODELING AND CHARACTERIZATION OF CAPACITIVE MICROMACHINED ULTRASONIC TRANSDUCERS

A DISSERTATION
SUBMITTED TO THE DEPARTMENT OF ELECTRICAL
AND ELECTRONICS ENGINEERING
AND THE INSTITUTE OF ENGINEERING AND SCIENCES
OF BİLKENT UNIVERSITY
IN PARTIAL FULFILLMENT OF THE REQUIREMENTS
FOR THE DEGREE OF
DOCTOR OF PHILOSOPHY

By
Ayhan Bozkurt
January 2000

TK
5982
.B69
2000

MODELING AND CHARACTERIZATION OF CAPACITIVE MICROMACHINED ULTRASONIC TRANSDUCERS

A DISSERTATION

SUBMITTED TO THE DEPARTMENT OF ELECTRICAL AND ELECTRONICS

ENGINEERING

AND THE INSTITUTE OF ENGINEERING AND SCIENCES

OF BILKENT UNIVERSITY

IN PARTIAL FULFILLMENT OF THE REQUIREMENTS

FOR THE DEGREE OF

DOCTOR OF PHILOSOPHY

By

Ayhan Bozkurt

January 5, 2000

TK
5982
.B69
2000

B052001

I certify that I have read this thesis and that in my opinion it is fully adequate, in scope and in quality, as a thesis for the degree of Doctor of Philosophy.

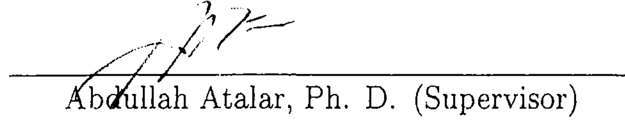

Abdullah Atalar, Ph. D. (Supervisor)

I certify that I have read this thesis and that in my opinion it is fully adequate, in scope and in quality, as a thesis for the degree of Doctor of Philosophy.

Hayrettin Köymen, Ph. D.

I certify that I have read this thesis and that in my opinion it is fully adequate, in scope and in quality, as a thesis for the degree of Doctor of Philosophy.

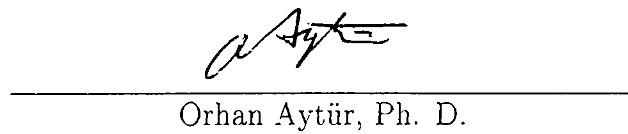

Orhan Aytür, Ph. D.

I certify that I have read this thesis and that in my opinion it is fully adequate, in scope and in quality, as a thesis for the degree of Doctor of Philosophy.

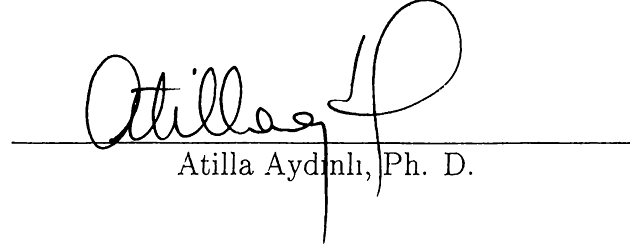

Atilla Aydınlı, Ph. D.

I certify that I have read this thesis and that in my opinion it is fully adequate, in scope and in quality, as a thesis for the degree of Doctor of Philosophy.

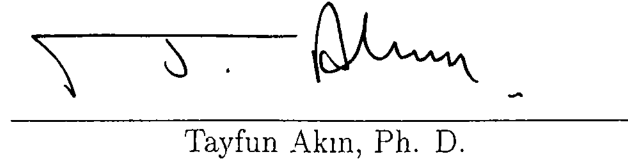

Tayfun Akın, Ph. D.

Approved for the Institute of Engineering and Sciences:

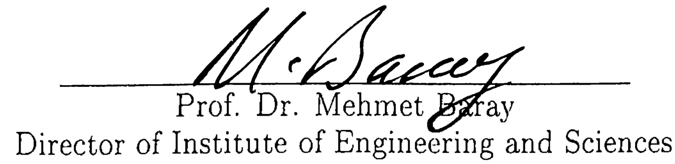

Prof. Dr. Mehmet Baray
Director of Institute of Engineering and Sciences

in loving memory of my father

ABSTRACT

MODELING AND CHARACTERIZATION OF CAPACITIVE MICROMACHINED ULTRASONIC TRANSDUCERS

Ayhan Bozkurt
Ph. D. in Electrical and Electronics Engineering
Supervisor: Prof. Abdullah Atalar
January 5, 2000

The Capacitive Micromachined Ultrasonic Transducer (cMUT) is a device used for the generation and detection of ultrasonic sound waves. The device is constructed on a silicon substrate using a microfabrication process. Individual cells constituting the device are membranes which have dimensions in the order of tens of microns, and are made up of a mechanically strong compound of silicon. The transducer itself has dimensions measured in centimeters, thus the total number of cells that make up a transducer is in the order of thousands. The excitation/detection of acoustic waves relies on the capacitance between the substrate and membrane: The presence of acoustic waves induces a small AC variation on the DC bias on the device, which can be used for detection, while a small AC component added to the DC bias by the drive circuit changes the electro-static attraction force on the membrane causing it to vibrate, producing acoustic waves. Basic advantages of cMUT devices include easy patterning of array structures, integration of drive/detection electronics with mechanical structures, and low cost.

In this study, basic theory describing the characteristics of cMUT devices were developed. The analytic formulation was used to test the validity of a Finite Element

Method (FEM) model. The FEM model, then, was employed in the analysis of structures for which no analytical models are present. Specific problems solved using the FEM model included the characterization of cMUT devices with judiciously patterned electrodes. A more specific study showed that the bandwidth of an immersion device with an active area of radius 25 μm can be increased by 100% by simply setting the electrode radius to 10 μm. The FEM analysis was, then, extended to handle the effects of substrate loss, which required the incorporation of an Absorbing Boundary Condition (ABC) into the model. A Normal Mode Theory analysis was conducted to give better insight to the physical nature of the effect of substrate loss to device characteristics. The dominant wavemode for a transducer of central frequency 2.5 MHz was found to be the lowest order anti-symmetric lamb wave mode (A0), for a silicon substrate of thickness 500 μm. A microfabrication process was developed for the production of cMUT devices. Hexagonally shaped transducers of radius 40 μm were fabrictated on a conducting silicon substrated with silicon nitride as the sacrificial layer and amorphous silicon as the membrane material. Both the gap and membrane thicknesses are set to 0.5 μm. 8, 16, and 24 μm gold plates were deposited as top eletrodes. The total number of active cells were 24 thousand for a substrate size of 0.7×0.7 cm^2. Some experimental results were obtained from the fabricated transducers to support the analytical cMUT model. The device is found to have a central frequency of 2 MHz.

Keywords : Capacitive Micromachined Ultrasonic Transducer (cMUT), Finite Element Method (FEM) Modeling, Absorbing Boundary Condition (ABC), Normal Mode Theory, Microfabrication Process.

ÖZET

KAPASİTİF MİKRO-İŞLENMİŞ ULTRASONİK ÇEVİRİCİLERİN MODELLENMESİ VE KARAKTERİZASYONU

Ayhan Bozkurt
Elektrik ve Elektronik Mühendisliği Doktora
Tez Yöneticisi: Prof. Dr. Abdullah Atalar
5 Ocak 2000

Kapasitif Mikro-işlenmiş Ultrasonik Çevirici (kMUÇ), ultrasonik ses dalgalarının üretilmesi ve algılanması için kullanılan bir cihazdır. Cihaz, silikon bir taban üzerinde mikro-fabrikasyon yöntemiyle üretilir. Cihazı oluşturan hücreler, boyutları on mikronlar mertebesinde olan ve silikonun mekanik olarak sağlam bir bileşiğinden yapılan zarlardır. Çeviricinin kendisi santimetre cinsinden ölçülebilen boyutlara sahip olduğu için bir çeviriciyi oluşturan toplam hücre sayısı binlerle ifade edilir. Akustik dalgaların uyarılması/algılanması, zar ile taban arasındaki kapasitansa dayanır: Akustik dalgaların varlığı, cihaz üzerindeki DC öngeriliminde algılama için kullanılabilecek küçük bir AC dalgalanmaya yol açarken, sürücü devre tarafından DC öngerilime eklenen küçük bir AC bileşen zar üzerindeki elektrostatik çekim kuvvetini değiştirerek zarı titreştirip akustik dalgalar üretir. Dizilim (array) yapılarının kolay biçimlendirilmesi, mekanik yapıların sürücü/algılama devreleriyle entegrasyonu ve düşük maliyet kMUÇ cihazlarının temel avantajları arasında yer almaktadır.

Bu çalışmada, kMUÇ cihazlarını karakterize etmekte kullanılan temel teoriler geliştirilmiştir. Analitik formulasyon, bir Sonlu Eleman Metodu (SEM) modelinin doğruluğunu

sınamak için kullanımıştır. SEM modeli, daha sonra analitik modeli bulunmayan yapıların analizinde kullanılmıştır. Elektrotları belli amaçlar için biçimlendirilmiş kMUÇ'ların analizi, SEM modeli kullanılarak çözülen özel problemler arasında yer almaktadır. Daha özel bir çalışma, sualtı uygulamaları için kullanılan 25 μm yarıçaplı bir cihazın elektrot yarıçapının 10 μm yapılmasıyla cihazın bant genişliğinin % 100 arttırılabileceğini göstermiştir. SEM analizi, daha sonra taban kayıplarını da içerecek şeklide genişletilmiştir. Bu, SEM modeline Emici Sınır Koşulları'nın (ESK) eklenmesini gerektirmiştir. Ayrıca bir Normal Mod Teorisi analiziyle problemin fiziksel temelinin daha iyi anlaşılabilmesi sağlanmıştır. Bu analizle, merkez frekansı 2.5 MHz ve taban kalınlığı 500 μm olan bir çevirici için hakim dalga modunun en düşük sıralı anti-simetrik Lamb dalgası modu olduğu tespit edilmiştir. Bu çalışmada ayrıca kMUÇ cihazlarının üretimi için bir mikrofabrikasyon yöntemi geliştirilmiştir. Bu yöntemle, zar malzemesi olarak amorf silikon, kalıp malzemesi olarak da silikon nitrat kullanılarak 40 μm çaplı altıgen biçimli çeviriciler üretilmiştir. Zar ve hava boşluğu kalınlıklarının her ikisi de 0.5 μm olarak seçilmiştir. Zarlar, elektrot olarak kullanılmak üzere 8, 16 veya 24 μm çaplı altın plakalarla kaplanmışlardır. 0.7×0.7 cm^2'lik bir çevirici alanı üzerinde 24 bin aktif hücre inşaa edilmiştir. Merkez frekansı 2 MHz olarak ölçülen çeviricilerden analitik kMUÇ modelini destekleyen ölçüm sonuçları alınmıştır.

Anahtar Sözcükler: Kapasitif Mikro-işlenmiş Ultrasonik Çevirici (kMUÇ), Sonlu Eleman Metodu (SEM), Emici Sınır Koşulları (ESK), Normal Mod Teorisi, Mikrofabrikasyon Yöntemi.

ACKNOWLEDGMENTS

I would like to express my sincere gratitude to Dr. Abdullah Atalar for his supervision, guidance, suggestions and encouragement through the development of this thesis.

I would like to thank to the members of my dissertation jury for reading the manuscript and commenting on the thesis.

I am indebted to Dr. Khuri-Yakub of the Ginzton Laboratory at Stanford University for providing the means for a summer internship. Many thanks are due to Dr. Değertekin and Dr. Ladabaum for their cooperation during my studies at the Ginzton Laboratory.

I would also like to thank to Dr. Ekmel Özbay for his support during the experimental work at the Physics Department. Special thanks go to Erhan Ata, Murat Güre, and Burak Temelkuran who have been my teachers in the clean room.

Endless thanks to Sanlı! Not only an excellent colleague, he has always been my most supporting friend.

And I would like to express my sincere gratitude to the following people: Güçlü, Bacar, Tolga, Gürkan, Uğur Oğuz, Gün, Lütfiye, for being my friends; Beygo, for giving life: Tünay, Hayri, Melis, for being there whenever I needed them; and Gülbin, for her endless support. Finally, like to thank to my parents, brother and Ebru, whose understanding made this study possible.

Contents

1 INTRODUCTION 1

1.1 Analysis 3

1.2 Experiment 5

2 ULTRASONIC TRANSDUCERS 6

2.1 The Micromachined Ultrasonic Transducer 6

2.2 Operational Principles and Parameters 9

3 ANALYTIC MODEL for cMUTs 10

3.1 Mason's Equivalent Circuit 10

3.2 cMUT Parameters: Collapse Voltage 12

3.3 cMUT Parameters: Bandwidth of Immersion cMUT 13

4 FEM MODELING OF cMUTs 15

4.1 Thermal and Electrostatic Analyses 16

4.2 Calculation of Electrostatic Pressure 17

4.3 ANSYS Modeling of cMUT 18

5 STATIC and DYNAMIC SIMULATION 20

5.1 Static Analysis 21

5.1.1 First Order Iteration (Small Deflection) 22

5.1.2 Static Analysis - Membrane Collapse Voltage 23

5.1.3 Static Analysis - Input Capacitance 25

5.2 Dynamic Analysis 26

5.2.1 Dynamic Analysis - Membrane Impedance 26

5.2.2 Dynamic Analysis - Electro-mechanical Transformer Ratio 26

6 OPTIMUM IMMERSION cMUT 29

6.1 Partially Metalized cMUT - Membrane Shape 31

6.2 Partially Metalized cMUT - Transformer Ratio 31

6.3 Partially Metalized cMUT - Simulation Results 34

6.3.1 Bandwidth of cMUT - Constant Bias 34

6.3.2 Bandwidth of cMUT - Variable Bias 35

7 cMUT LOSS MODELING 38

7.1 FEM Model for Substrate Coupling 39

7.2 Acoustic Impedance of cMUT with Loss 42

7.3 cMUT Loss vs. Model Dimensions 46

7.4 Normal Mode Theory Analysis 47

8 **DEVICE FABRICATION** **54**

8.1 An Introduction to Microfabrication 54

8.2 cMUT Fabrication 55

8.3 Device Dimensions 63

8.4 SEM Images 65

8.5 Experimental Setup 67

8.6 Measurement Results 70

8.7 Discussion and Further Work 72

9 **CONCLUSION** **73**

A **A MICROMACHINING GLOSSARY** **76**

B **MATERIAL PARAMETERS** **78**

List of Figures

2.1 Schematic views of two silicon cMUT structures. 7

2.2 3D visualizations for various cMUT structures. 8

3.1 Equivalent electrical circuit for the cMUT membrane. 11

4.1 Metal object surrounded by medium of dielectric constant ϵ. 18

4.2 ANSYS Model of Circular MUT. 19

4.3 Finite element mesh of the model geometry. 19

5.1 Application of temperature on model geometry. 21

5.2 Structural loads on model geometry. 22

5.3 Clamped MUT membrane model. 22

5.4 E-filed intensity (left) and membrane deflection (right) for V=100 Volts. 23

5.5 Steps of iterative electrostatic-structural solution. 24

5.6 Iteration results for a stable and a collapsing membrane. 25

5.7 Acoustic impedance of membrane with zero residual stress. 27

6.1 Reduced electrical circuit for the cMUT membrane. 29

6.2 Electro-mechanical transformer ratio, capacitance and bandwidth of cMUT transducer for electrode radius ranging from 2 to 24 μm. 34

6.3 Butterworth network for electrical matching. 35

6.4 Normalized transducer bandwidth for two electrode sizes. 36

6.5 Collapse voltage values for varying electrode sizes. 36

6.6 Transducer bandwidth for DC bias equal to the collapse voltage. 37

7.1 Cross-sectional view of cMUT structure. 39

7.2 Finite-element model of the cMUT. 40

7.3 Magnitude of nodal displacement on substrate (Left 1.0, Right 3.0 Mhz). 41

7.4 Fitted curve on ANSYS damp parameter determined by trial-and-error. . 42

7.5 Impedance of cMUT with substrate loss (real and imaginary parts) 42

7.6 Real impedance for a point contact. 43

7.7 Submodeling I : Substrate impedance. 43

7.8 Real substrate impedance for circular excitation. 44

7.9 Two-port representation for the cMUT membrane. 44

7.10 Submodeling II : Membrane as a two-port. 45

7.11 Forces at the rim of the membrane. 45

7.12 cMUT Impedance: unified and two-part models 46

7.13 Real part of cMUT impedance for various substrate thicknesses. 47

7.14 Lowest (0th) order symmetric and antisymmetric plate modes (S0 and A0). 47

7.15 Dispersion curves for A0 and S0 modes in the frequency range 1.0–3.0 MHz 49

7.16 Particle velocity field distribution (A_0 and FEA) at 1 MHz (r_1=29.9 mm). 50

7.17 Total power coupled to the substrate and powers for A_0 and S_0 modes. 51

7.18 Equivalent circuit model which includes cMUT substrate loss. 51

7.19 Total loss resistance of cMUT and resistances of A_0 and S_0 modes. 52

7.20 Equivalent circuit model revisited: modal loss accounts for total loss. 53

8.1 Process steps 1, 2a, 2b, 2c, 2d and 3. 58

8.2 Process steps 4a, 4b, 4c, 4d, 4e and 5a. 59

8.3 Process steps 5b and 5c. 60

8.4 Top view of cMUT structure for various fabrication steps. 60

8.5 Zoomed view of mask (active membrane area 500×250 μm^2 approx.). 63

8.6 Basic building block used in drawing the cMUT mask. 64

8.7 SEM images of fabricated cMUT devices. 66

8.8 Experimental setup for cMUT characterization. 67

8.9 Detection circuit for cMUT. 68

8.10 Ginzton detection circuit for cMUT. (courtesy Dr. Sanlı Ergun) 69

8.11 Real and imaginary parts of cMUT impedance for various bias voltages. . 70

8.12 Simplified model for cMUT with ohmic losses. 71

8.13 Experimental results and model data. 71

List of Tables

4.1 Analogous field and material quantities 16

7.1 Device dimensions for the analyses. 39

8.1 Equipment used in cMUT fabrication 55

8.2 Chemicals used in sample cleaning 56

8.3 Process charts 1–4 61

8.4 Process charts 5–8 62

8.5 cMUT fabrication process parameters. 64

8.6 Shunt input capacitance of cMUT as a function of electrode radius. 71

Chapter 1

INTRODUCTION

The generation and detection of ultrasonic waves has long been a concern in many fields of technology which include imaging, a general name for applications ranging from medical ultrasound to underwater acoustics; and nondestructive evaluation (NDE), which covers a huge set applications such as flow measurement, material characterization, detection of holes/cracks/fractures, assessment of bonding quality of layered material, etc. In almost all applications, piezo-electric transducers were the unique choice, as alternatives such as capacitive transducers did not perform well when compared to their ultrasonic counterparts. Air-coupled and immersion capacitive ultrasonic transducers had long existed [1–3] and their characteristics and performance had been exhaustively evaluated. However, until recent developments in micromachining techniques which have led to the design of new versions of the devices [4–10], those were not considered as serious alternatives for piezo-electric transducers.

Piezo-electric transducers exploit a physical phenomenon called "piezoelectricity": an electric field causes a crystal structure to change its shape, or reversely, a crystal produces an E-filed when it's shape is changed. Capacitive ultrasonic transducers, on the other hand, use electrostatic forces: changing the charge on the plates of a capacitor

changes the mutual attraction force, causing the plates to displace. Likewise, a change in the plate displacement, when the voltage is held constant, causes a current to flow either out from, or in to the capacitor. A capacitive Micromachined Ultrasonic Transducer, is a collection of thousands of small capacitors with one plate being in the form of a free-to-vibrate membrane, each cell having dimensions in the order of tens of microns.

Capacitive Micromachined Ultrasonic Transducers (cMUT), have the same qualities of the piezo-electric transducers, when power output, dynamic range and operation frequency are concerned. However, there are three basic advantages associated with cMUTs which deserve mentioning: First, they perform better in air. Materials used in the fabrication of piezo-electric transducers usually have acoustic impedances in the order of 30×10^6 kg/m^{2}s, 5 orders of magnitude higher than that of air (400 kg/m^{2}s). There has been a great effort in the development of matching layers, but these did not produce satisfactory results as either materials with desired acoustic impedances were not available, or the matching layer was required to be impractically thin, or the matched transducer turned out to have a a very narrow band. However, proper adjustment of design parameters for cMUTs result in transducers that perform quite well even at frequencies as high as 11.4 MHz [6]. A second advantage is about the convenience in fabrication of complicated structures, such as array transducers. Piezo-electric array transducer production requires the use of fine mechanical processing tools, and employs a cumbersome wiring step to connect the transducer to drive/detection electronics. For cMUTs, however, structures are pattered using standard lithography, which makes the fabrication of fancy structures quite convenient, and the drive electronics can be even constructed on the same substrate, removing the necessity for wiring. Third, silicon processing is a widely available well-established method. Therefore, cMUT devices are fabricated very cheaply.

Theories explaining the electro-mechanical properties of piezo-electric transducers have been well established, and the behavior of fabricated transducers can be precisely

predicted. Unfortunately, the same does not apply to cMUTs. Some theory and analysis methods explaining their operation have been proposed [4, 7, 11–13]. Still, the behavior of these devices require comprehensive analysis and design parameters must be well evaluated. As main motivational forces behind transducer development include applications in air-coupled NDE, new structures for efficient ultrasonic transmission into air need to be developed. Likewise, designs for 3-D immersion imaging using 2-D transducer matrices require a good understanding of coupling between array elements. Furthermore, for all applications, sources of mechanical loss need to be evaluated, as the spectral characteristics of the device are greatly affected by loss.

This study has two focus points: the development of analysis tools for the evaluation of cMUT characteristics, and the experimental verification of proposed analysis methods. For the first objective, a lumped circuit representation for the cMUT device was developed by the help of numerical analysis tools. For the second, a microfabrication process was developed and implemented in a clean room environment. We now discuss both parts of the thesis in more detail:

1.1 Analysis

The basic analysis method to evaluate the performance of micromachined structures is to use an electrical equivalent circuit and express evaluation criteria in electrical terms such as insertion loss, or electrical bandwidth. Mason proposed an lumped electrical equivalent circuit for capacitive transducers [14]. This model has been extensively used in our analyses to verify numerical results. Chapter 3 describes Mason's model in detail.

Mason's model describing cMUT characteristics only applies to particular device structure. Real-life structures, however, usually do not satisfy conditions to make the Mason's model valid. As there are no closed form expression describing the behavior of those devices, numerical methods need to be employed. Chapter 4 describes how the

cMUT device is modeled using the Finite Element Model (FEM) and how eletrostatic and mechanical FEM probems can be coupled.

The FEM model proposed in Chapter 4 is first used to regenerate the results of Mason, and was found to produce correct results, as described in Chapter 5. Simulation for real-life structures are run and results are assessed by comparing them to heuristic expectations. Simulations are then extended to accurately work out device parameters (e.g., the collapse voltage) which are just estimated by Mason's model.

One parameter of significance is the bandwidth of the transducer which, basically, determines the pulse response of the device. Part of this study focuses on the bandwidth optimization of immersion transducers, using analysis tools developed in Chapter 5. Although electrode patterning has been used for selective mode excitation of resonators, [15] and in the optimization of capacitive pressure transducers and microphones [16], there is no comprehensive study in the literature on the performance optimization of capacitive micromachined ultrasonic transducers (cMUTs) using electrode patterning. In Chapter 6 we present optimization criteria, analyses, and simulations which demonstrate that electrode patterning can be used to significantly enhance the performance of cMUTs.

Power coupled to anywhere other than the loading medium is considered as a loss term for a transducer.The basic loss mechanism for capacitive micromachined ultrasonic transducers is the power coupled to the substrate. Surface wave modes on solid half-spaces and acoustic waveguides have been extensively studied [17]. The power coupled to these nodes can be determined by matching the stress amplitude at the membrane rim to the wave amplitudes of these nodes. Consequently, loss can be incorporated into the lumped model of the cMUT. The same analysis can be used to determine cross-coupling to neighboring transducer elements. The amount of loss and cross-coupling is significant in the determination of transducer bandwidth and array performance. Chapter 7 finds out values for loss terms to be incorporated in Mason's model. A modal theory analysis is included to give better insight to the physical nature of coupling to surface wave modes.

1.2 Experiment

Chapter 8 discusses a microfabrication process developed for the production of cMUT devices. There are well established fabrication processes reported in literature [4, 6, 18–20]. Here, we mimic the Stanford fabrication process described in [20], but we use our own mask design and process sequencing, and make use of equipment available in the Advanced Research Laboratory of the Physics Department of Bilkent University. The fabricated devices are found to have reasonable electrical performance, despite their low reliability. Although the experiments do not provide full support to the analytic results, they still provide good insight to the fabrication techniques, and their electrical characteristics are well explained by a very basic model which is the starting point of the entire modeling work.

All of the analyses described in Chapters 5 and 6 assume a transducer of circular shape, as an FEM model for a circular structure is easily generated. However, the fabricated transducers are of hexagonal shape to allow close packing. This will have an insignificant effect on device characteristics, and the analysis for a circular transducer will apply to the hexagonal structure.

To summarize, research work described in this thesis includes:

- Electrical Modeling of Capacitive Micromachined Ultrasonic transducers
- Optimization of device characteristics using electrode patterning.
- Modeling of mechanical losses using both FEM analysis results and mode theory.
- Development of a microfabrication process for the production of cMUT devices.

Chapter 2

ULTRASONIC TRANSDUCERS

Ultrasonic transducers are devices capable of converting electrical signals into ultrasound and vice versa. They find wide application in the fields of non-destructive evaluation and medical imaging. Advances in microfabrication techniques enabled the construction of micromachined versions of these devices with significant advantages described in this chapter.

2.1 The Micromachined Ultrasonic Transducer

The almost universally used transducer type is that constructed using piezoelectric materials [17]. Though being very commonly used, piezoelectric transducers have low conversion efficiency and their operation is limited to relatively low frequencies, because of mechanical limitations on the production of small devices. For improved system performance and high resolution imaging, efficient high frequency transducers are required. Capacitive Micromachined Ultrasonic Transducers (cMUTs), perform much better than their piezoelectric counterparts in terms of the mentioned figures of merit. Micromachined ultrasonic transducers [8,11,12,21], are produced using standard silicon processes

and are distinguished with their efficiency, strength and reliability.

Fig. 2.1 shows the cross-sectional view of two different cMUT devices. The device in the upper schematic has a vibrating membrane consisting of silicon nitride, supported by a silicon oxide layer. A thin gold layer is plated to act as an electrode. The silicon

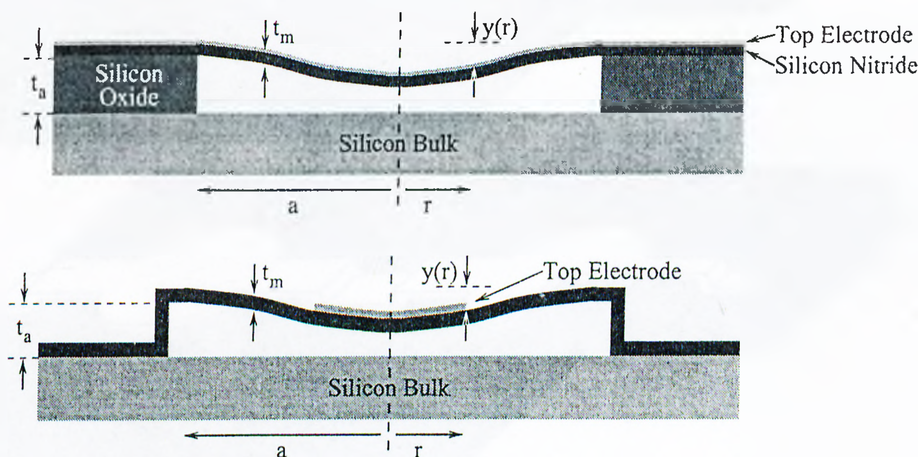

Figure 2.1: Schematic views of two silicon cMUT structures.

substrate on which the device is constructed is the second electrode. The device's mechanical action is due to the electrostatic attraction force between the two electrodes. The device is circular, the dashed line in the figure showing its axis of rotation. The central cavity into which the membrane can deflect is vacuumed. The vibrating membrane of the device in the lower schematic is supported by the silicon nitride layer itself.

Fig. 2.2 shows 3-D visualizations for various cMUT structures. The top figure corresponds to the upper drawing in Fig. 2.1: the membrane layer is supported by the sacrificial layer from which cylindrical openings are cut. The upper layer is made slightly transparent to show the gap. For the structures shown in the central and lower drawings, the membrane is formed by shaping the membrane layer itself: at certain regions the membrane material is raised to form a gap. This gap can be either circular, as in the central drawing, or hexagonal (lower figure), latter of which results in more closely packed membranes. All drawings show two membranes with circular top electrodes placed at

their centers and interconnected with metallic stripes.

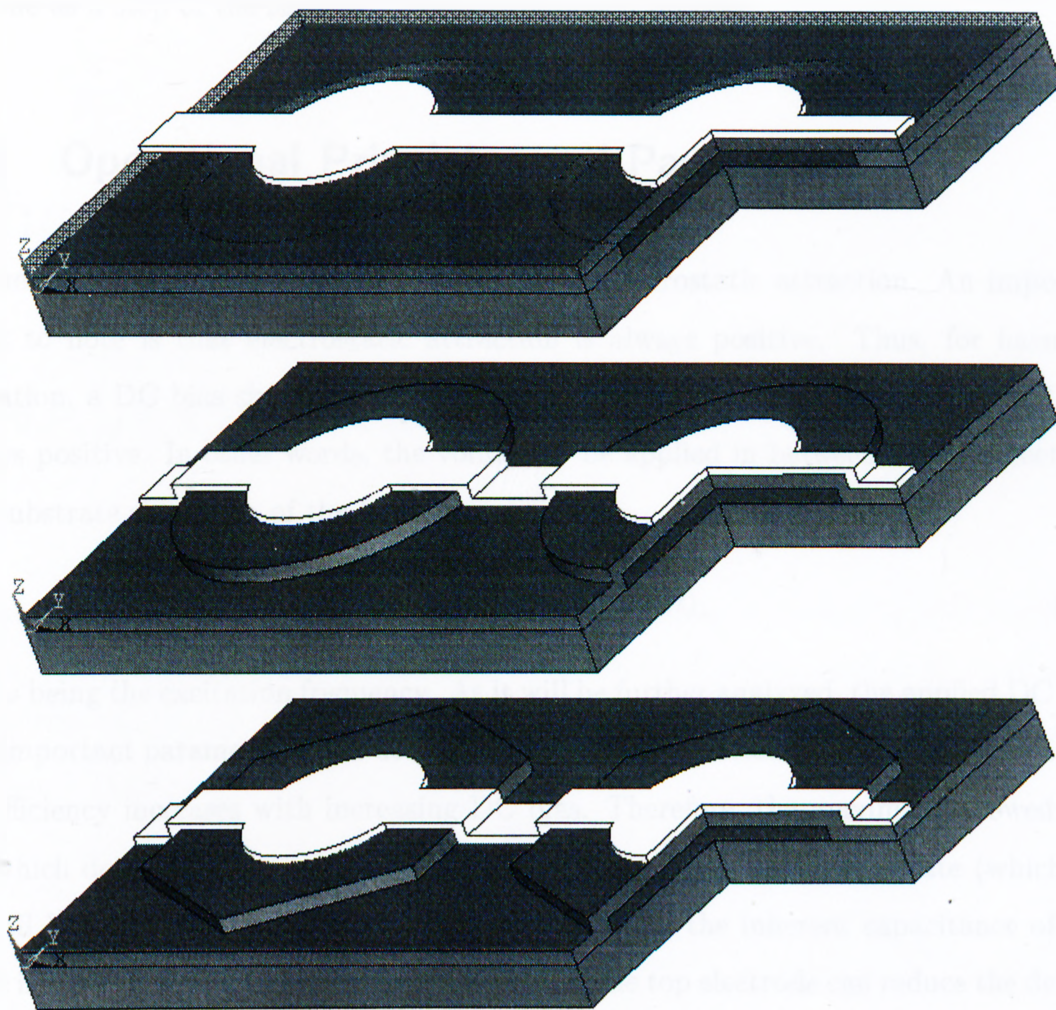

Figure 2.2: 3D visualizations for various cMUT structures.

The production technique involved in the fabrication of the latter structure will be described in Chapter 8.

One obvious advantage of capacitive transducers constructed using a micromachining process is that the accompanying electronics can be constructed on the same substrate on which the device resides. This results in noise immunity (as the cabling between the transducer and driving/receiving electronics is eliminated) and ease of production (e.g., no flat parallel cables are required to be connected to array elements). Many foundries

now offer mixed micromachining/electronics processes for which the micromachining part is done as a step of the standard device production process.

2.2 Operational Principles and Parameters

As mentioned, the cMUT's activation is due to electrostatic attraction. An important point to note is that electrostatic attraction is always positive. Thus, for harmonic operation, a DC bias should be applied to make sure that the voltage on the cMUT is always positive. In other words, the voltage to be applied in between the top electrode and substrate should be of the form

$$V(t) = V_{DC} + V_{AC}\sin(\omega t) \tag{2.1}$$

with ω being the excitation frequency. As it will be further analyzed, the applied DC bias is an important parameter which determines the device's efficiency. The effect is positive, i.e., efficiency increases with increasing DC bias. Therefore, the maximum allowed DC bias which does not causes the membrane to collapse down to the substrate (which we will call $V_{collapse}$) is of importance. On the other hand, the inherent capacitance of the device is another design consideration. Patterning the top electrode can reduce the device capacitance, but this reduces the device efficiency. However, capacitance and efficiency have complex dependencies on electrode shape. Thus, an optimum point for device performance can be found by judiciously patterning the top electrode. Simulation results showing the validity of the last argument will be presented in the following chapters.

Chapter 3

ANALYTIC MODEL for cMUTs

In this chapter, we describe the model used in the analysis of capacitive micromachined ultrasonic transducers (cMUT) and present some theoretically derived parameters of the device. The theoretical derivations are verified by simulations which will be described in subsequent chapters.

3.1 Mason's Equivalent Circuit

The analysis of the cMUT structure is based on the equivalent circuit approach of Mason [14] as adapted in [4]. The model, as seen in Fig.3.1, consists of a shunt input capacitance C_0 at the electrical port and an electro-mechanical transformer with turns ratio $1 : n$. Z_a is the lumped acoustic impedance of the membrane and Z_l is the acoustic load, which is just the acoustic impedance of the medium Z_{medium} multiplied by the membrane area $S_{membrane}$. V and i show the input voltage and current, respectively. F is the total electrostatic force on the membrane under the assumption that electrostatic pressure is uniform at all points. For the lumped model, the measure for the membrane movement is its average velocity v.

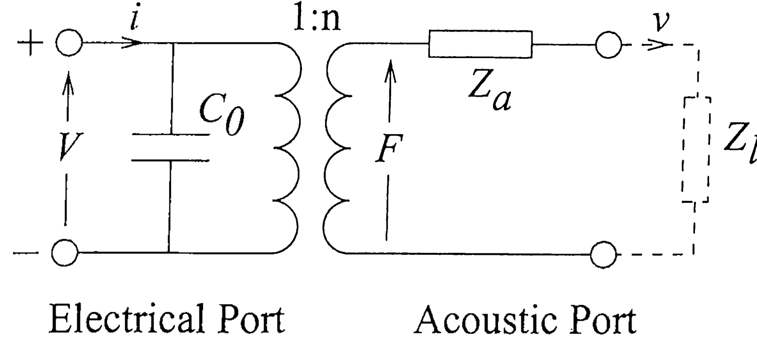

Figure 3.1: Equivalent electrical circuit for the cMUT membrane.

According to Mason [14], the membrane deflection is described by the differential equation

$$\frac{(Y_0 + T)t_n^3}{12(1-\delta^2)}\,\nabla^4 y - t_n\,T\,\nabla^2 y - P + t_n\,\rho\,\frac{\partial^2 x}{\partial t^2} = 0 \tag{3.1}$$

where t_n is the membrane thickness, T is the residual stress in the membrane material, Y_0 is the Young's modulus, δ is the Poisson's ration, ρ is density and P is the applied pressure. For harmonic excitation, we have

$$\frac{(Y_0 + T)t_n^3}{12(1-\delta^2)}\,\nabla^4 y - t_n\,T\,\nabla^2 y - P - \omega^2 t_n\,\rho\,x = 0 \tag{3.2}$$

where ω is the frequency. Boundary conditions for a clamped diaphragm are

$$y(r)|_{r=a} = 0; \qquad \left.\frac{\partial dy}{\partial dr}\right|_{r=a} = 0. \tag{3.3}$$

Solving eqn. 3.2 with the above boundary conditions we get

$$y(r) = \frac{P}{\omega^2 \rho t_n}\left[\frac{k_2 I_1(k_2 a)J_0(k_1 r) \;+\; k_1 J_1(k_1 a)I_0(k_2 r)}{k_2 J_0(k_1 a)I_1(k_2 a) \;+\; k_1 J_1(k_1 a)I_0(k_2 a)} - 1\right] \tag{3.4}$$

with

$$k_1 = \sqrt{\frac{\sqrt{d^2 + 4c\omega^2} - d}{2c}}; \quad k_2 = \sqrt{\frac{\sqrt{d^2 + 4c\omega^2} + d}{2c}} \tag{3.5}$$

where

$$c \triangleq \frac{(Y_0 + T)t_n^2}{12(1-\delta^2)}; \qquad d \triangleq \frac{T}{\rho t_n}. \tag{3.6}$$

This solution assumes that pressure P has constant amplitude for all r. The equation for $y(r)$ will be used to justify simulation results. The average velocity $v(\omega)$ of the membrane

is

$$v(\omega) = j\omega 2\pi \int_0^a r\, y(r)\, dr. \tag{3.7}$$

Substituting the above expression for $y(r)$, the membrane impedance $Z_a = (\pi a^2)P/v(w)$ is found as

$$Z_a = \frac{j\omega\rho t_n}{\pi a^2} \left[\frac{\left[k_2 \frac{J_0(k_1 a)}{J_1(k_1 a)} + k_1 \frac{I_0(k_2 a)}{I_1(k_2 a)}\right] \frac{k_1 k_2 a}{2(k_1^2+k_2^2)}}{\left[k_2 \frac{J_0(k_1 a)}{J_1(k_1 a)} + k_1 \frac{I_0(k_2 a)}{I_1(k_2 a)}\right] \frac{k_1 k_2 a}{2(k_1^2+k_2^2)} - 1} \right]. \tag{3.8}$$

This expression for Z_a will be used to check the membrane impedance found by simulations. Furthermore, equation Z_a yields an analytic expression for the resonance frequency of the cMUT membrane.

3.2 cMUT Parameters: Collapse Voltage

When the DC bias voltage applied to the membrane exceeds a critical value, the membrane collapses over the silicon membrane. This critical voltage ($V_{collapse}$) can be found by modeling the membrane as a parallel plate capacitor suspended above a fixed ground plate with a linear spring. The spring constant (κ) can be found as the ratio of pressure to volume displacement: [14]

$$\kappa = \frac{T\, A\, t_n}{\left(\frac{c}{d} - \frac{a}{2}\frac{J_0(a\sqrt{d/c})}{J_1(a\sqrt{d/c})}\sqrt{\frac{c}{d}} + \frac{a^2}{8}\right)} \tag{3.9}$$

where

$$c = \frac{(E+T)t_n^2}{12\rho(1-\sigma^2)}; \quad d = \frac{T}{\rho} \tag{3.10}$$

with T, ρ and σ being the residual stress, density and Poisson's ratio of the membrane material, and A being the area of the membrane. If x denotes the membrane displacement, the total restoring string force is

$$F_S = \kappa x \tag{3.11}$$

The electrostatic force on the membrane is given by

$$F_E = \frac{A\epsilon^2 V^2}{2\epsilon_0 \left(t_n + \frac{\epsilon}{\epsilon_0}(t_a - x)\right)^2}. \tag{3.12}$$

The voltage to keep the membrane at a certain deflection x can be found by equating F_E to F_S and solving for V. The critical voltage at which the membrane becomes unstable can be determined by finding the displacement for which $\partial V/\partial x = 0$. Solving yields

$$x = \frac{1}{3}\left(t_a + \frac{\epsilon_0}{\epsilon} t_n\right) \tag{3.13}$$

and the corresponding collapse voltage is found as

$$V_{collapse} = \sqrt{\frac{8\kappa \left(t_a + \frac{\epsilon_0}{\epsilon} t_n\right)^3}{27A\epsilon_0}}. \tag{3.14}$$

3.3 cMUT Parameters: Bandwidth of Immersion cMUT

If the cMUT transducer is assumed to be a parallel plate capacitor, its capacitance is

$$C_0 = \frac{\epsilon\, A}{\left(t_n + \frac{\epsilon}{\epsilon_0} t_a\right)}. \tag{3.15}$$

For small deflections of the membrane,

$$E(r,t) = V(t)/(t_n + \frac{\epsilon}{\epsilon_0} t_a) \tag{3.16}$$

Thus,

$$T(r,t) = \frac{1}{2}\frac{\epsilon^2}{\epsilon_0}(V_{DC}^2(r) + 2\, V_{DC}(r) V_{AC}(r) \sin\omega t)/(t_n + \frac{\epsilon}{\epsilon_0} t_a)^2 \tag{3.17}$$

and the electro-mechanical transformer ratio n (which is the time varying part of T(r,t) times the membrane area divided by the AC voltage) is

$$n = A\,\frac{\epsilon^2}{\epsilon_0}\, V_{DC}\, \frac{1}{(t_n + \frac{\epsilon}{\epsilon_0} t_a)^2} \tag{3.18}$$

Consequently, the RC time constant τ of the transducer (which is given as $\tau = C_0 Z_l / n^2$) is

$$\tau = \frac{\epsilon_0^2}{\epsilon^3}\frac{1}{V_{DC}^2}\left(t_n + \frac{\epsilon}{\epsilon_0}t_a\right)^3 Z_l. \tag{3.19}$$

Eq. 3.14 contains the spring constant κ of the membrane as a term, which is has an approximate expression [14]

$$\kappa = \frac{16\,\pi\,Y_0\,t_n^3}{(1-\rho^2)a^2}. \tag{3.20}$$

Substituting this into the collapse voltage expression of Eq. 3.14, we get

$$V_{collapse} = \sqrt{\frac{128\,Y_0\,t_n^3\,(t_n + \frac{\epsilon}{\epsilon_0}t_a)^3}{27\,\epsilon_0\,(1-\rho^2)\,a^4}}. \tag{3.21}$$

Combining Equations 3.19 and 3.21 yields the expression for the time constant

$$\tau = Z_w \frac{27\,(1-\rho^2)}{128\,Y_0}\,\frac{a^4}{t_n^3} \tag{3.22}$$

where Z_w is the acoustic impedance of the loading medium. This equation shows that the bandwidth of the cMUT does not depend on the air gap thickness when V_{DC} is at $V_{collapse}$.

The resonance frequency f_c of the cMUT membrane is [14]

$$f_c = \frac{(2.4)^2}{2\pi}\sqrt{\frac{Y_0}{12\rho(1-\delta^2)}}\,\frac{t_n}{a^2}. \tag{3.23}$$

If a cMUT is to operate at a certain frequency, t_n/a^2 has to be constant when adjusting device dimensions to increase bandwidth. This condition, when combined with Eq. 3.22 implies that the device bandwidth linearly increases with increasing membrane thickness t_n.

Chapter 4

FEM MODELING OF cMUTs

Usually, complex mechanical structures cannot be analyzed using analytic models. In those cases, the Finite Element Method (FEM) can be employed to obtain numerical solutions to problems. Theoretical derivations for the behavior of clamped circular membranes [14] allow the evaluation of a single type of transducer geometry. For different geometries and boundary conditions simulations are run using ANSYS Rev.5.2 [22–25].

The FEM software package ANSYS is unable to handle static electrical problems. However, many commercially available FEM packages (including ANSYS) are able to solve field problems of the Laplace and Poisson type, which include heat conduction problems. Although, not usually stated in software references, these programs are able to solve electrostatic field problems, as well. The analogy between the governing differential equations of these two types of problems enables a direct substitution of corresponding field and material quantities [26].

We first present the theoretical tools employed in the simulations and then explain how the cMUT was modelled using ANSYS.

4.1 Thermal and Electrostatic Analyses

In heat conduction, Poisson's equation describes a problem in which the temperature distribution Γ is to be solved from a known heat generation $\dot{q}$ in a medium of known heat conduction k, which turns out to be

$$\nabla^2\Gamma = -\dot{q}/k \tag{4.1}$$

for an isotropic medium. The electrostatic counterpart of this equation, the field quantity to be determined is the scalar potential ϕ given the charge distribution ρ in a region of permittivity ϵ, which, in turn, is

$$\nabla^2\phi = -\rho/\epsilon \tag{4.2}$$

again for an isotropic medium. An immediate observation of Eqns. 4.1 and 4.2, and further noting that the scalar potential is related to the electric field intensity E by $E = -\nabla\phi$, suggest the following table for analogous field and material quantities (viz. table 4.1). The only consideration when making substitutions for the listed field and

Thermal	Electrical
k (conductivity)	ϵ (permittivity)
Γ (temperature)	ϕ (scalar potential)
$\dot{q}$ (heat generation)	ρ (charge density)
$\nabla\Gamma$ (temperature gradient)	$-E$ (electric field intensity)

Table 4.1: Analogous field and material quantities

material quantities is that corresponding quantities for the thermal and electrical problems should be in the same system of units. The solution data should be interpreted accordingly, as well.

4.2 Calculation of Electrostatic Pressure

The total force acting on a volume charge distribution ρ due to an external electric field $\mathbf{E}$ is given by

$$\mathbf{F} = \int \mathbf{F}_v dV \tag{4.3}$$

where $\mathbf{F}_v$ is the volume density of force, defined as

$$\mathbf{F}_v = \rho \mathbf{E} \tag{4.4}$$

The force expression given in Eqn. 4.3 is a function of both field and charge. According to the Faraday-Maxwell field theory, force can be expressed as a function of the field only, as force is transmitted by means of the field. This suggests the existence of a force function $\boldsymbol{\Upsilon}$ on the surface enclosing the volume in consideration such that

$$\int_V \mathbf{F}_v dV = \int_S \boldsymbol{\Upsilon} dS \tag{4.5}$$

where $\boldsymbol{\Upsilon}$ is called the Maxwell Stress Tensor. After some vector manipulation, the expression for $\boldsymbol{\Upsilon}$ is found as

$$\boldsymbol{\Upsilon} = \epsilon_0 \left[(\mathbf{n} \cdot \mathbf{E})\mathbf{E} - \frac{E^2}{2}\mathbf{n} \right] \tag{4.6}$$

where $\mathbf{n}$ is the surface normal. For a rigorous derivation, the reader is advised to refer to [27], pp.112-113. Consider now that we have a metallic object of arbitrary shape, placed in a non-conducting medium with electric permittivity ϵ. We would like to find an expression for $\boldsymbol{\Upsilon}$, noting that this problem requires additional treatment as Eqn. 4.6 is for a non-dielectric medium. Before proceeding, we observe that $\mathbf{E}$ is perpendicular to the object surface (i.e., $\mathbf{E} = E\mathbf{n}$), so that $\mathbf{n} \cdot \mathbf{E} = E$. Hence, if the metal object were in vacuum, the expression for $\boldsymbol{\Upsilon}$ would be

$$\boldsymbol{\Upsilon} = \epsilon_0 \frac{E^2}{2}\mathbf{n} \tag{4.7}$$

However, the object is surrounded by a medium of permittivity ϵ. Consider that we have an infinitesimally thin layer of vacuum between the object surface and the enclosing

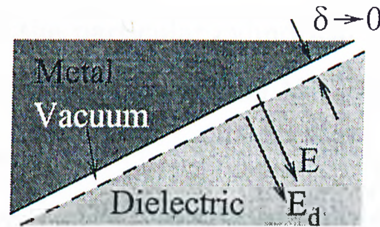

Figure 4.1: Metal object surrounded by medium of dielectric constant ϵ.

medium, as depicted in Fig. 4.1. From the Gauss' flux theorem, $\mathbf{E} = (\epsilon/\epsilon_0)\mathbf{E}_d$, where $\mathbf{E}$ and $\mathbf{E}_d$ are electric field vectors in vacuum and dielectric, respectively. Combining this with Eqn. 4.7 results in

$$\Upsilon = \frac{\epsilon^2}{\epsilon_0}\frac{E_d^2}{2}\mathbf{n} \tag{4.8}$$

which is the desired stress expression for the metal object in dielectric.

4.3 ANSYS Modeling of cMUT

ANSYS supports the modeling of **Thermal** and **Structural** elements. One ANSYS element type of this category is SOLID13 which can be used individually as an element having thermal or structural degrees of freedom, or it can be employed in an analysis where the effects of both are coupled. Throughout the work presented, the former analysis type is used as the thermal model is employed just to work out the solution of the electrical problem, and thermo-structural effects, such as thermal expansion, have nothing to do with the problem in hand. Hence, the structural and thermal (i.e., electrical) problems are handled separately and their coupling is provided by "artificial" means, which will be the discussed in the following sections.

The MUT whose static and dynamic electro-mechanical properties are to be investigated is modeled as a two dimensional axisymmetric solid. Elements of this type basically define a volume of rotation around the y-axis. Thus, rectangles with one edge aligned with the y-axis model cylinders, and the view on the computer screen turns out to be a

side view of a slice cut out of the particular cylindrical object to be modeled. Fig. 4.2 depicts the two dimensional model for the silicon MUT to be analyzed. All regions are

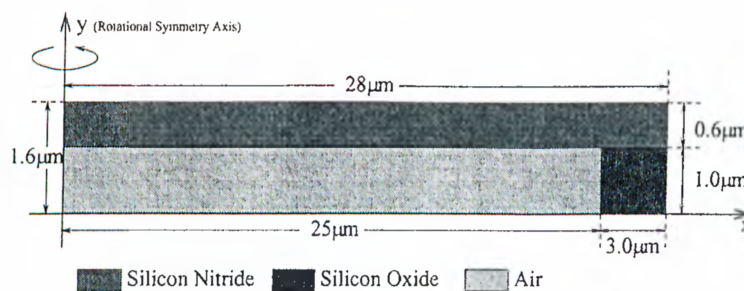

Figure 4.2: ANSYS Model of Circular MUT.

bound to each other at boundaries. The air layer is modeled using a solid element, too. It is there just to provide a coupling medium for the electrical FEM analysis, and as it has low stiffness, low density, it does not perturb the structural solution. The actual membrane has a very thin gold layer on top of the Si_3Ni_4 layer as an electrode, whose effect can be safely ignored for the structural analysis. Therefore it is not included in the FEM. Likewise, the whole structure lies on a silicon substrate, which will be modeled by defining structural boundary conditions. Electrical potential will be input to the model by defining nodal temperatures at the top and bottom lines (planes).

The next step in the FEM analysis of the cMUT is meshing. Fig. 4.3 shows a coarse

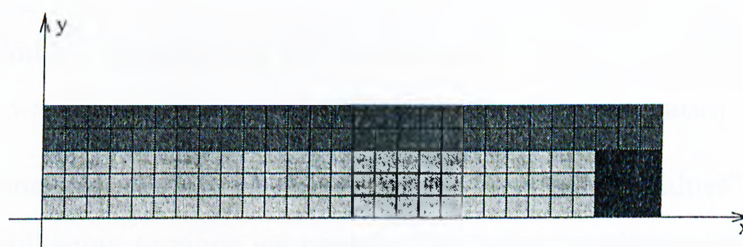

Figure 4.3: Finite element mesh of the model geometry.

version of the mesh used in simulations. As the element type used in simulations has both degrees of freedom, thermal and structural solutions are obtained using the same mesh. The number of mesh divisions are adjusted to have reasonable accuracy.

Chapter 5

STATIC and DYNAMIC SIMULATION

The static (DC) and dynamic (harmonic) simulations of the cMUT are done separately as ANSYS does not support a combined structural analysis. The static analysis of the cMUT membrane yields

- The shape and capacitance of the device for an applied DC bias,
- The collapse voltage ($V_{collapse}$),
- E-filed values to be used in the dynamic analysis.

The dynamic analysis, using results of the DC solution, provides

- The mechanical impedance of the membrane,
- The electro-mechanical conversion efficiency (transformer ratio).

Results of both analyses are then used to determine "component values" of the equivalent circuit. In the following sections we present simulation results together with analytic figures to show the accuracy of the FEM model.

5.1 Static Analysis

The static displacement of the membrane is of interest in the determination of the shunt input capacitance, the collapse voltage and field quantities for the harmonic analysis. All of these require the determination of the membrane shape for an applied DC voltage. The static analysis of the membrane deflection is done by first solving the electrostatic problem, then computing the resulting pressure and finally performing a structural analysis to find the effect of electrostatic forces on the structure. It is apparent that once structural deformation occurs, the electrostatic solution is altered, which is the source of the deformation. Therefore, the problem is non-linear in nature which calls for an iterative solution. Once the structural deformation is found, the electrostatic problem should be solved once again, followed by another structural analysis, and so on. In each analysis step, the Thermal package of ANSYS is used to find the electrostatic field for a certain metalization size. Fig. 5.1 shows the application of thermal loads to the undeflected model geometry. E-field intensity at the electrode-membrane boundary is

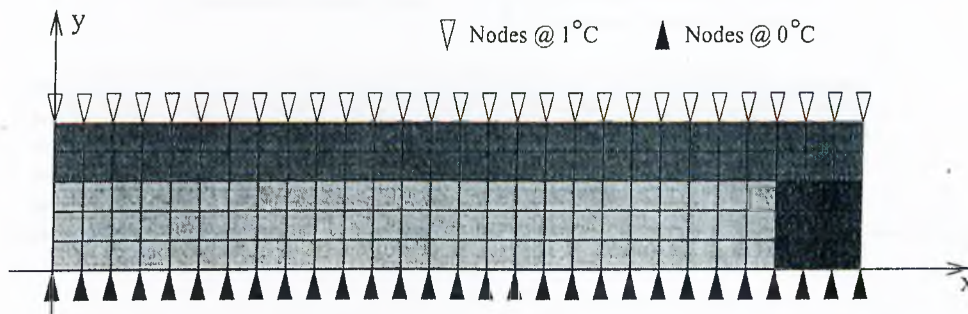

Figure 5.1: Application of temperature on model geometry.

found by computing the thermal gradient. Then, we employ the Maxwell Stress Tensor equation (5.1) to find the electrostatic pressure on the membrane:

$$\Upsilon_{DC}(r) = \mathrm{n}\frac{\epsilon^2}{2\epsilon_0}E_{DC}^2(r). \tag{5.1}$$

The computed pressure values are, then, applied as structural loads to the model geometry as depicted in Fig. 5.2.

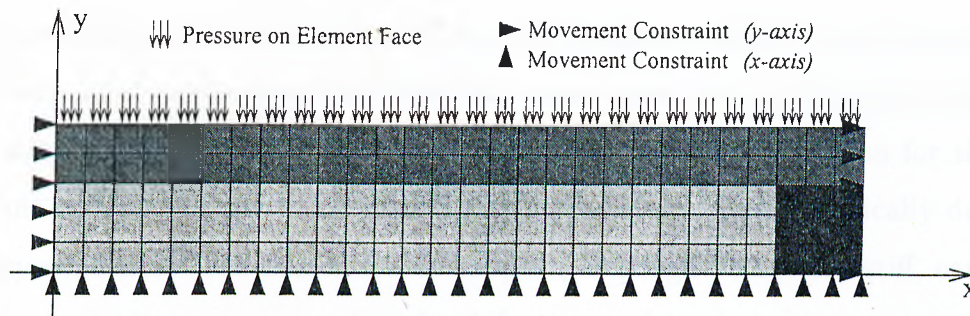

Figure 5.2: Structural loads on model geometry.

5.1.1 First Order Iteration (Small Deflection)

The accuracy of first order simulation results is tested by comparing the simulated deflection data with results of analyses from theory [14]. Mason, in his model, assumes that the membrane's end is clamped and the applied pressure is uniform on the membrane surface. The ANSYS model for the MUT has no clamping at the membrane ends. To test the validity of out model, modifications depicted in fig. 5.3 has been made. Here,

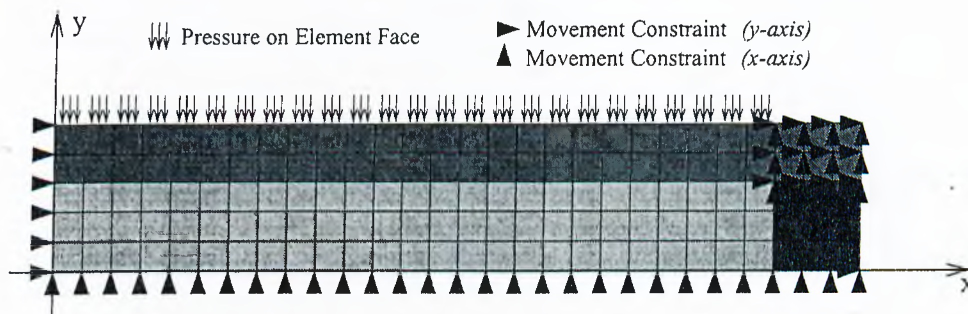

Figure 5.3: Clamped MUT membrane model.

the membrane is clamped right at the start of the support and all pressure components are set to have a constant value. Hence, simulation conditions are set as close as to the assumptions of the derived equations.

The results are striking. Fig. 5.4 shows the analytic membrane deflection together with two simulation results; one for a clamped membrane and the other for a free one, the latter being a better result when judged by closeness to reality. The simulation result

for the clamped membrane shows that the model produces results in excellent agreement with theory, as it can be seen from the plot, and a closer look at numerical data shows that results are correct within the third decimal digit. The simulation for the "real" membrane deflects slightly more than theory's prediction. This is basically due to the boundary condition. The Silicon Oxide support, although being very stiff, can still be compressed, yielding non-zero values for deflection and its derivative at the membrane boundary. Moreover, electric field intensity gets higher at the upper electrode - Silicon Nitride boundary as going away from the center of the membrane towards the supported part of it (see fig. 5.4).

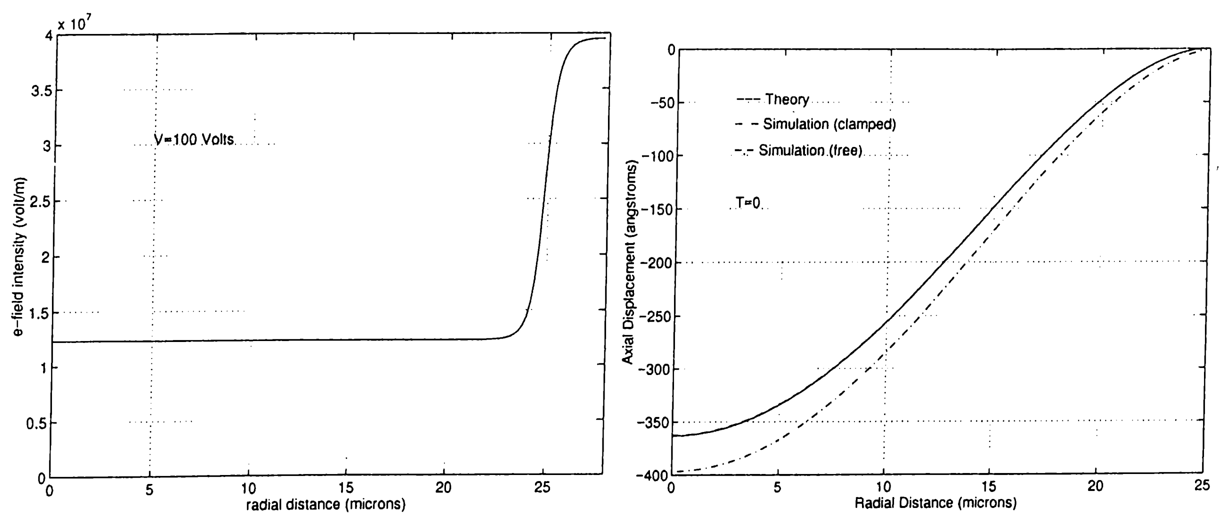

Figure 5.4: E-filed intensity (left) and membrane deflection (right) for V=100 Volts.

5.1.2 Static Analysis - Membrane Collapse Voltage

As mentioned at the very beginning of the section on static analysis, structural changes affect the electrostatic problem and, hence, an iterative solution is required to determine the membrane shape for larger deflections. The problem is not very involved. Once the deflection is determined, the electrostatic problem is re-solved. The new set of elemental pressure values is then used to find a new structural solution. The iteration continues

until either an infinitesimal change occurs in shape or the membrane collapses. Fig. 5.5 shows a flow-chart describing the iteration, where ϵ is the stopping criteria, d is the height of the air gap and $y(r)$ is the membrane deflection at a radial distance r. The

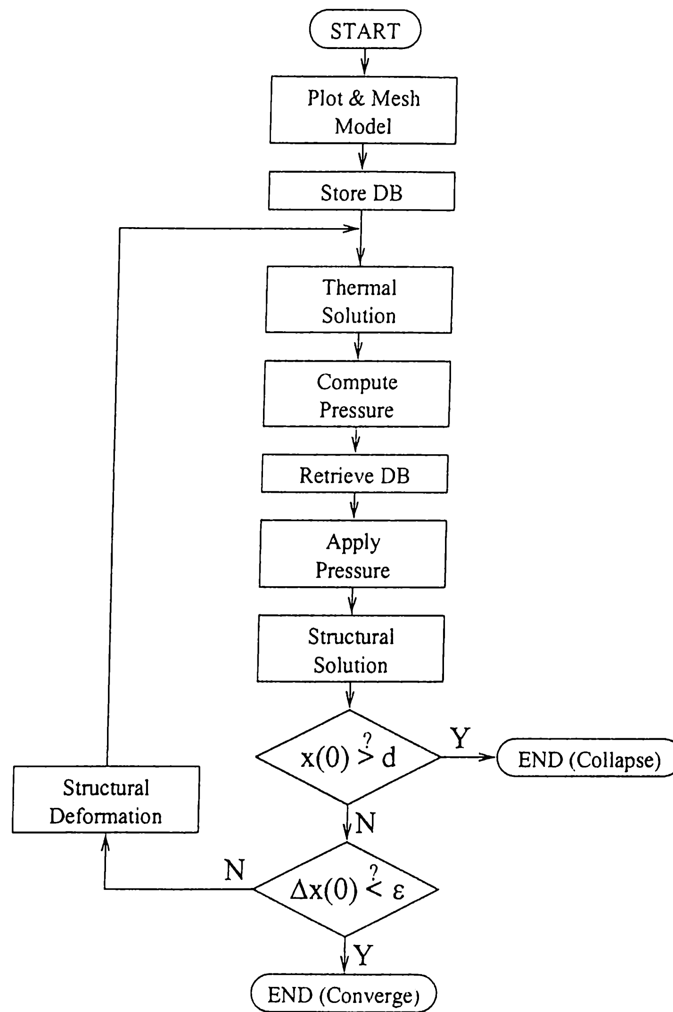

Figure 5.5: Steps of iterative electrostatic-structural solution.

iteration to determine the membrane shape is terminated either when the membrane shape stabilizes or when the membrane collapses onto the substrate. For the former case the applied voltage is lower than the collapse voltage, while for the latter case the applied voltage is above the collapse voltage. The collapse voltage is the value of the DC bias at which the membrane is infinitesimally close to collapse. Figure 5.6 shows iteration results for a stable and collapsing membrane, respectively. The applied voltages are 230

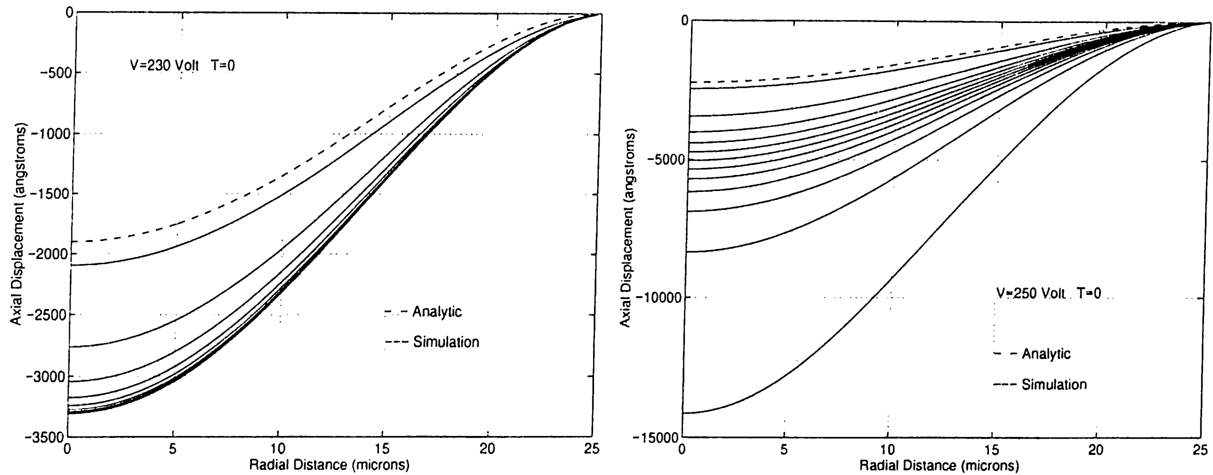

Figure 5.6: Iteration results for a stable and a collapsing membrane.

and 250 Volts. The collapse voltage for this particular membrane is some value between these voltages. The trace labeled "Analytic" is the result of the analytical treatment assuming uniform deflections and forces.

5.1.3 Static Analysis - Input Capacitance

The results of the static analysis are used to determine the shunt input capacitance $C_0(V_{DC})$[1] of the transducer. For a certain DC bias voltage, the shape of the membrane is determined by the iterative simulation described above. Once the electric field intensity at the deflected membrane surface is known, the charge distribution on the electrode is found using Gauss' Theorem. The capacitance of the membrane for various electrode sizes is determined by computing the total charge on the membrane and dividing this by the applied voltage. So, if $E_{DC}(r)$ is the electric field intensity, $C_0(V_{DC})$ is given by

$$C_0(V_{DC}) = \frac{\epsilon}{V_{DC}} \oint_S \mathbf{E}_{DC} \cdot ds = \frac{2\pi\epsilon}{V_{DC}} \int_0^a r\, E_{DC}(r)\, dr. \qquad (5.2)$$

[1] C_0 is a function of the DC bias voltage V_{DC} because the membrane shape is determined by V_{DC}.

5.2 Dynamic Analysis

The aim of the dynamic (harmonic) analysis is the determination of additional model parameters of the equivalent electrical circuit: the lumped acoustic impedance of the membrane Z_a, and the electro-mechanical transformer ratio n.

5.2.1 Dynamic Analysis - Membrane Impedance

The acoustic impedance Z_a of the membrane is found by first finding $v(\omega)$ for zero acoustic load (i.e., the cMUT in vacuum) and a uniform excitation pressure at the set of frequencies of interest, and then dividing the total force on the membrane by these velocity values. The accuracy of the analysis is tested by comparing the simulated impedance values to analytical results. Mason [14], in his formulation of the membrane's mechanical behavior, assumes that the membrane ends are clamped. The same boundary conditions are imposed during simulations for test purposes. For the stated boundary conditions, there is a remarkable match between the analytical and numerical results. The actual membrane's ends are not clamped; rather, they rest on the sacrificial oxide layer. Simulation results for this case show that the resonance frequency of the actual membrane is slightly less than that of the clamped membrane. Fig. 5.7 shows the two simulation results together with the analytic impedance curve.

5.2.2 Dynamic Analysis - Electro-mechanical Transformer Ratio

As previously stated,electrostatic forces generated by a voltage are always attractive, regardless of the polarity of the applied voltage. Hence, a voltage of the form

$$V(t) = V_{DC} + V_{AC} \sin \omega t \tag{5.3}$$

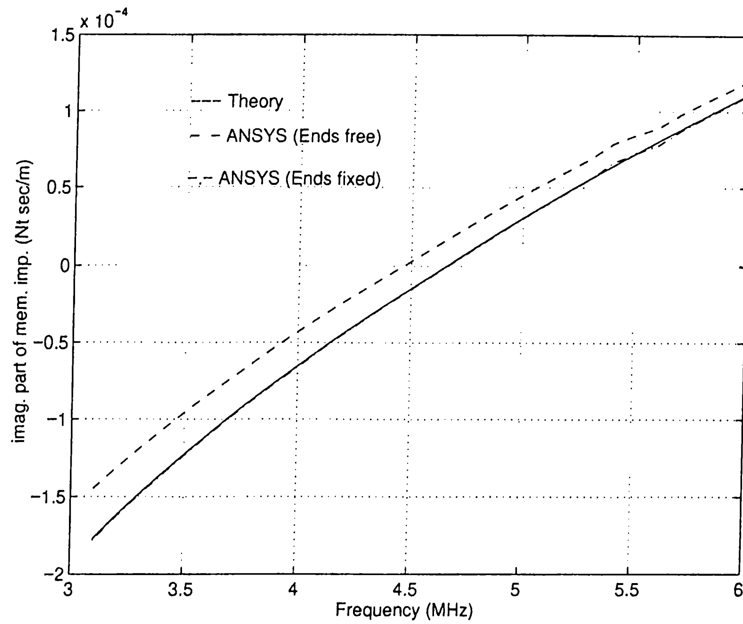

Figure 5.7: Acoustic impedance of membrane with zero residual stress.

with $V_{DC} \gg V_{AC}$ is applied to the membrane to assure harmonic motion. The applied DC bias V_{DC} will cause the membrane to deflect towards the substrate. We assume that V_{AC} results in a small harmonic motion compared to the DC deflection and also assume that the cMUT membrane behaves like an ideal plate capacitor so that uniform E-field exist on the membrane surface. The, the resulting electric field intensity is

$$E(r,t) = E_{DC} + E_{AC} \sin \omega t \tag{5.4}$$

with r being the radial distance from the membrane's center, $E_{DC}(r)$ the E-field intensity at the membrane-electrode boundary for the DC bias, and

$$E_{AC} = \frac{V_{AC}}{V_{DC}} E_{DC}. \tag{5.5}$$

The electrostatic pressure on the membrane can be found using the Maxwell Stress Tensor equation

$$\Upsilon(t) = \mathbf{n} \frac{\epsilon^2}{\epsilon_0} \frac{E^2(t)}{2} \tag{5.6}$$

where $\mathbf{n}$ is the surface normal of the metal electrode and ϵ is the relative permittivity of the membrane material. Substituting Eq. 5.4 into Eq. 5.6 and ignoring second order

terms gives the temporal and spacial variation of electrostatic pressure on the cMUT surface:

$$\Upsilon(t) = \mathbf{n}\frac{\epsilon^2}{2\epsilon_0}E_{DC}^2 + \mathbf{n}\frac{\epsilon^2}{\epsilon_0}E_{DC}E_{AC}\sin\omega t \tag{5.7}$$

The total AC force F_{AC} on the membrane is

$$F_{AC} = (\pi a^2)\frac{\epsilon^2}{\epsilon_0}E_{DC}E_{AC} = A\frac{\epsilon^2}{\epsilon_0}V_{DC}V_{AC}\left(t_n + \frac{\epsilon}{\epsilon_0}t_a\right)^{-2} \tag{5.8}$$

and consequently the electro-mechanical transformer ratio is

$$n \;=\; F_{AC}/V_{AC} \;=\; A\frac{\epsilon^2}{\epsilon_0}V_{DC}\left(t_n + \frac{\epsilon}{\epsilon_0}t_a\right)^{-2} \tag{5.9}$$

The electro-mechanical transformer ratio, n, determines by how much the effect of the mechanical properties of the membrane are reflected to the electrical port, as shown in Fig. 3.1.

Chapter 6

OPTIMUM IMMERSION cMUT

When the cMUT is used as an immersion device (i.e., loaded with a relatively high acoustic impedance liquid such as water) the acoustic impedance of the cMUT membrane Z_a and the load Z_l form a low quality factor circuit. In such cases, the membrane impedance can be neglected for frequencies near the mechanical resonance of the device. The equivalent circuit, then, reduces to a simpler network containing Z_l, C_0 and the electro-mechanical transformer. Fig. 6.1 shows the reduced model for the cMUT used as

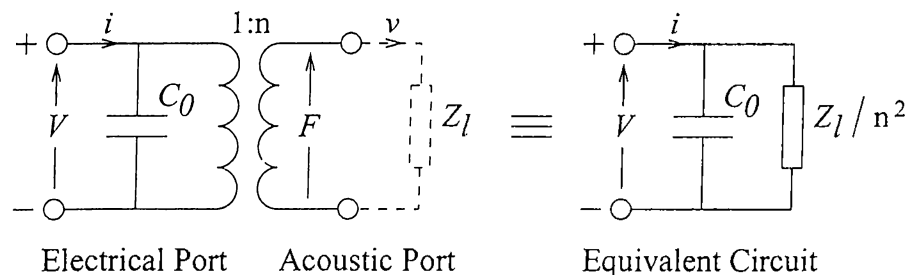

Figure 6.1: Reduced electrical circuit for the cMUT membrane.

an immersion device. Here, we limit our discussion to the effect of the shunt capacitance C_0 on the efficiency and bandwidth of the device. If bandwidth were not a concern, one could simply tune out C_0 with an inductor to achieve zero insertion loss. But bandwidth is indeed a concern, so a more complete formulation of the optimization objective is to

minimize the time constant, τ, of the first order network formed by the shunt input capacitance and the transformed radiation impedance, where $\tau = C_0 \, Z_l \, / \, n^2$. One might suggest that decreasing the metalization for the top electrode can help to reduce the capacitance without any sacrifice from electromechanical properties, i.e., by reducing the top electrode size, C_0 can be reduced without reducing the electromechanical conversion efficiency, n. This argument is based on the idea that how much the membrane deflects depends not only on how much force is applied, but also on where this force is applied. It seems that pushing the membrane at parts close to its boundary does not help much as it its supported there by a relatively stiff layer. The point is to apply force to that part by which the membrane can be more easily deflected, which, by common sense, is its center. As it will be justified by simulation results, this argument is valid, and a smaller electrode result in a cMUT with higher bandwidth.

In order to find the bandwidth of the transducer for a certain electrode size, we need to compute the electro-mechanical transformer ratio n, and the input capacitance C_0. The following is a step-by-step task list describing the computation of n and C_0:

1. Find out the membrane shape for the applied DC bias.
2. Find E_{DC} for the membrane under DC deflection, and
    - 2.1. Integrate E_{DC} over the electrode to find C_0.
    - 2.2. Compute E_{AC} by scaling E_{DC}.
3. Compute Υ_{AC} from E_{AC} and perform a harmonic analysis.
4. Find average membrane velocity.
5. Find AC force by multiplying average velocity and membrane impedance.
6. The fraction of the AC force and applied AC voltage will yield n.

6.1 Partially Metalized cMUT - Membrane Shape

Determining the membrane shape is done by making use of the iterative method described in the chapter on simulations. The only difference is that for the partially metalized membrane, force appears on only a fraction of the membrane, not on its whole surface as it used to be. C_0 is to be found as in the static analysis section.

6.2 Partially Metalized cMUT - Transformer Ratio

Qualitatively, the transformer ratio relates the current and voltage at the electrical port to the velocity and force at the acoustic port, and that its value depends on the electrode pattern. The subtlety lies in the fact that the velocity and force of the acoustic ports are lumped parameters of a system which is in reality distributed. The force, as defined in the derivation of the equivalent circuit [4,14], is a uniform force over the entire membrane, and the velocity is defined as the average of the velocities on the contour of the membrane. Given that the electrostatic force is not uniform, especially in the case of partially metalized electrodes, consistency with the equivalent circuit model requires that the lumped electrostatic force (F in Fig. 3.1) be interpreted as an effective force. This effective force ($F_{effective}$) is the force which, if applied uniformly over the entire membrane, would give the same peak membrane displacement that the patterned electrode gives. To find the electro-mechanical transformer ratio n in a dynamic analysis, one needs to compute the average membrane velocity corresponding to an applied voltage V_{AC} with no acoustic load, multiply that with Z_a to find $F_{effective}$ and then divide $F_{effective}$ by the applied voltage:

$$n_{partial} = \frac{F_{effective}}{V_{AC}} = \frac{vZ_a}{V_{AC}} \tag{6.1}$$

So, again, we assume that a voltage of the form

$$V(t) = V_{DC} + V_{AC} \sin \omega t \tag{6.2}$$

with $V_{DC} \gg V_{AC}$ is applied to the membrane to assure harmonic motion. The applied DC bias V_{DC} will cause the membrane to deflect towards the substrate. We assume that V_{AC} results in a small harmonic motion compared to the DC deflection so that the resulting electric field intensity is

$$E(r,t) = E_{DC}(r) + E_{AC}(r)\sin\omega t \tag{6.3}$$

with r being the radial distance from the membrane's center, $E_{DC}(r)$ the E-field intensity at the membrane-electrode boundary for the DC bias, and

$$E_{AC}(r) = \frac{V_{AC}}{V_{DC}} E_{DC}(r). \tag{6.4}$$

Again, we employ the Maxwell Stress Tensor equation, which is

$$\Upsilon(r,t) = \mathbf{n}\frac{\epsilon^2}{\epsilon_0}\frac{E^2(r,t)}{2}. \tag{6.5}$$

Substituting Eq. 6.3 into Eq. 6.5 and ignoring second order terms gives the electrostatic pressure on the cMUT surface:

$$\Upsilon(r,t) = \mathbf{n}\frac{\epsilon^2}{2\epsilon_0}E_{DC}^2(r) + \mathbf{n}\frac{\epsilon^2}{\epsilon_0}E_{DC}(r)E_{AC}(r)\sin\omega t \tag{6.6}$$

Combining Eq. 6.4 and Eq. 6.6, the AC pressure on the cMUT $\Upsilon_{AC}(r,t)$ surface is found as

$$\Upsilon_{AC}(r) = \frac{\epsilon^2}{\epsilon_0}\frac{V_{AC}}{V_{DC}}E_{DC}^2(r) \tag{6.7}$$

Thus, if E_{DC} is known, this can be used to compute the AC excitation for the harmonic analysis. The harmonic analysis will yield nodal displacement (or equivalently velocity) values for the membrane surface. This can be used to compute the average velocity of the membrane, namely

$$v(\omega) = \frac{1}{A}\int_0^a 2\pi r\,\omega\,x_{AC}(r)\,dr. \tag{6.8}$$

Multiplying $v(\omega)$ with $Z_a(\omega)$ yields the effective total force $F_{effective}(\omega)$ on the cMUT membrane. The electromechanical transformer ratio n is, then, given by

$$n = \frac{F_{effective}(\omega)}{V_{AC}} \tag{6.9}$$

It should be pointed out that n has a negligible frequency dependence as long as only the primary vibration mode of the membrane is possible. For verification, simulations were run at two frequencies (one being smaller than ω_c and the other greater), and the same values for n were found.

An important point to note here is that Z_a is a mechanical property associated with the cMUT membrane; it is not altered with changing electrode size or with loading. Thus, we first find Z_a for particular device dimensions, and use this value for all subsequent analyses of varying electrode sizes. The electro-mechanical transformer ratio, n, is a function of metalization radius and thus has to be calculated for each individual electrode size. It is also important to note that for the analyses herein presented, the actual value of Z_a is not very significant because it is dwarfed by the magnitude of Z_l; rather, the value of $n_{partial}$, for a given Z_a, due to electrode minimization is important. The following section presents more detail about the finite element simulations and quantitatively demonstrates that electrode patterning can indeed improve cMUT performance in the specific case of circular membranes.

6.3 Partially Metalized cMUT - Simulation Results

Two sets of simulations for the bandwidth of the cMUT are run: First, a constant DC bias voltage is assumed. Secondly, the DC bias is set close to the collapse voltage, which is a function of electrode size.

6.3.1 Bandwidth of cMUT - Constant Bias

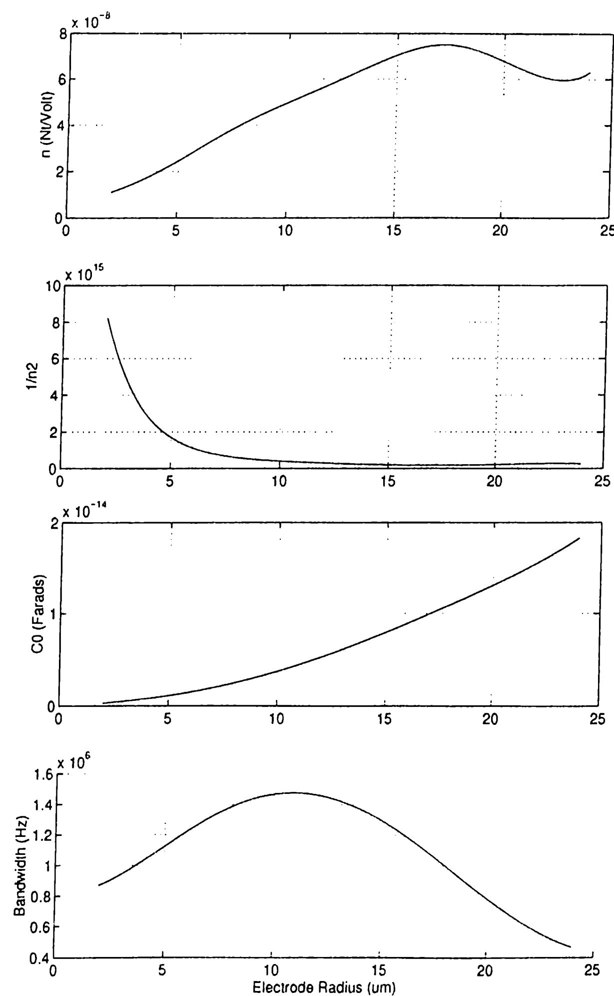

Figure 6.2: Electro-mechanical transformer ratio, capacitance and bandwidth of cMUT transducer for electrode radius ranging from 2 to 24 μm.

The electro-mechanical transformer ratios for various electrode sizes are determined

by running structural simulations and computing the average membrane velocity under harmonic excitation. These results are used to find the effective force on the membrane and, consequently, the electro-mechanical transformer ratios. In Fig. 6.2, plots of n, $1/n^2$, C_0 and the bandwidth of the resulting RC network (which is $1/\tau_{partial}$) are given. The last graph indicates that with the proposed criteria, a transducer of dimensions shown in Fig. 4.2, is optimized by an electrode of 11 μm radius.

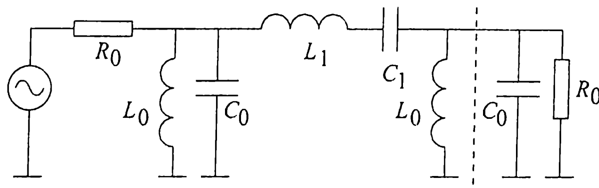

Figure 6.3: Butterworth network for electrical matching.

For the purpose of electrical matching we select a lossless matching network topology to tune out the parasitic element (C_0) of the transducer equivalent circuit [28, 29]. The sixth order maximally flat (Butterworth) network [30] shown in Fig. 6.3 is used for the electrical matching. C_0 is set equal to the shunt input capacitance of the transducer, the source resistance is chosen as equal to the radiation resistance of the transducer, and the center frequency of the network is set to the mechanical resonance frequency of the membrane. The remaining component values are computed by properly scaling the values in the prototype network of [30], which are also found in various Butterworth tables of radio handbooks. The resulting bandwidth of the transducer for two different metal electrode sizes is depicted in Fig. 6.4. For both electrode sizes, the DC bias voltage is assumed to be 200 Volts. This is less than the voltage that causes the fully metalized membrane to collapse, which is found as 240 Volts by simulations.

6.3.2 Bandwidth of cMUT - Variable Bias

The analysis method described in the static analysis of the cMUT has been used to determine the collapse voltage for varying electrode sizes. Figure 6.5 shows the simulation

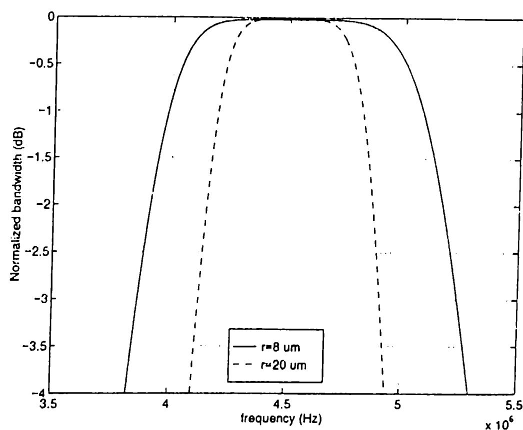

Figure 6.4: Normalized transducer bandwidth for two electrode sizes.

results for the device of figure 4.2. Because the total force on the membrane scales with

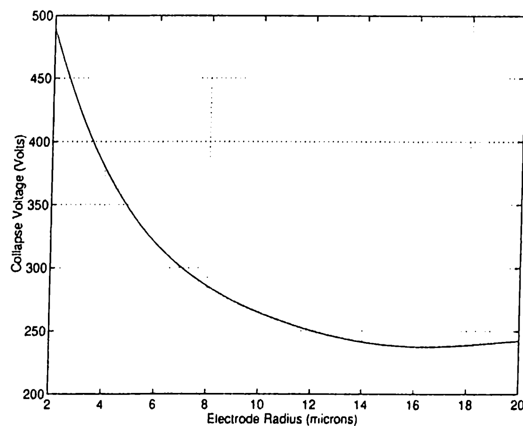

Figure 6.5: Collapse voltage values for varying electrode sizes.

electrode area, a higher voltage is required for the collapse of a membrane with a smaller electrode. Thus, for a smaller electrode a larger bias can be applied. From Eq. 6.7 we see that AC stress on the membrane increases with increasing DC bias[1]. If the membrane is modeled as a linear spring, we expect the AC deflection to be linearly dependent to T_{AC}. Thus, for increasing DC bias, the effective force on the membrane increases. This results in a larger value for n and, consequently, a larger bandwidth. So if the DC bias is set to the collapse voltage, the bandwidth of the transducer further increases for smaller

[1]The dependency is close to linear for small deflections as E_{DC} linearly scales with V_{DC}. However, for larger deflections, E_{DC} increases faster as the membrane gets closer to the substrate.

electrodes. Fig. 6.6 shows the bandwidth of the transducer of Fig. 4.2 as a function of electrode radius when the bias is set to the collapse voltages shown in Fig. 6.5. According

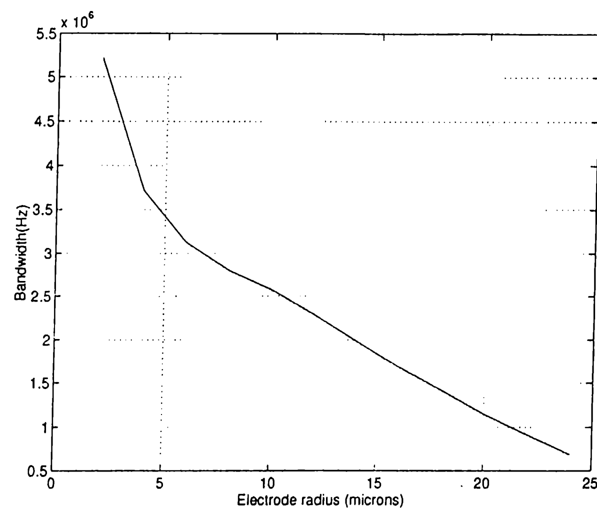

Figure 6.6: Transducer bandwidth for DC bias equal to the collapse voltage.

to this result, the transducer with maximum bandwidth should have a top electrode as small as possible. Interconnections to the top electrode will set a limit on how small it can get, as will breakdown mechanisms.

Chapter 7

cMUT LOSS MODELING

The main breakthrough brought about by cMUT devices is due to the inherent advantages of the technology used in the production: silicon processing enables convenient integration between the mechanics and electronics, and provides the designer with tools for easily patterning mechanical structures - quite important for the production of array transducers. At the same time, the method of production brings about an important issue regarding the performance of cMUT devices: the cMUT consists of cells that have dimensions in the order of tens of microns [9], and as a transducer of reasonable size has dimensions expressed in millimeters, thousands of individual devices need to be placed on the same substrate [18]. Consequently, an individual transducer cell, instead of being clamped at its ends, resides on a large substrate and couples power to radially outward wave modes. Furthermore, this power is received by the neighboring transducer elements creating cross-coupling between individual cells of the transducer. Although a model explaining the behavior of a single cell has been proposed, the above mentioned power loss and cross-coupling effects still remain unexplained. As main motivational forces behind transducer development include applications in air-coupled nondestructive evaluation (NDE), analysis methods that include the loss mechanisms in cMUTs need to be developed for the design of efficient transducers for ultrasonic transmission

into air. Likewise, designs for 3-D immersion imaging using 2-D transducer matrices require a good understanding of coupling between array elements. All of these call for the development of models close to reality: models that incorporate power coupled to the substrate.

In this chapter, we develop a simulation model to determine the mechanical impedance of a cMUT device that includes the effect of power coupled to the substrate. Finite Element Method models are used in conjunction with absorbing boundary conditions.

7.1 FEM Model for Substrate Coupling

The cMUT under analysis is considered to have a structure as depicted in Fig. 7.1. The following device dimensions have been used throughout the analyses (Table 7.1):

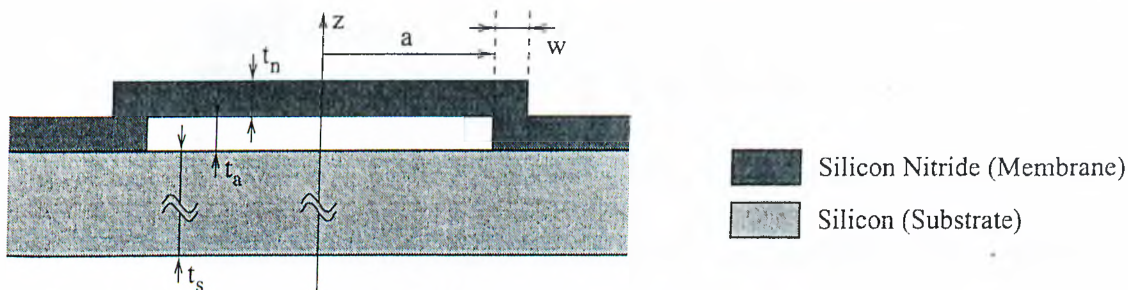

Figure 7.1: Cross-sectional view of cMUT structure.

The listed dimensions results in a device whose first order resonance is at 2.3MHz.

Parameter	Symbol	Value
Membrane thickness	t_n	1.0 μm
Airgap thickness	t_a	1.0 μm
Substrate thickness	t_s	500.0 μm
Membrane Radius	a	45.0 μm

Table 7.1: Device dimensions for the analyses.

The primary concern in the analysis is to find out the radially outward flowing power

coupled by the membrane into the substrate. For this, we need to have an absorbing boundary at the radial edges of our model. Levander [31] and Cerjan *et al.* [32] have used lossy material boundaries to absorb waves incident on model boundaries. Later, Berenger's [33] Perfectly Matched Layer (PML) for electromagnetic waves was shown to be applicable to elastic wave propagation problems by Chew *et al.* [34] and was used in a number of applications [35–37]. In this study, we use a lossy medium of considerable length to absorb the outward propagating waves. Fig. 7.2 depicts the finite element model involved in the analysis. The attenuation in the lossy part of the model has to

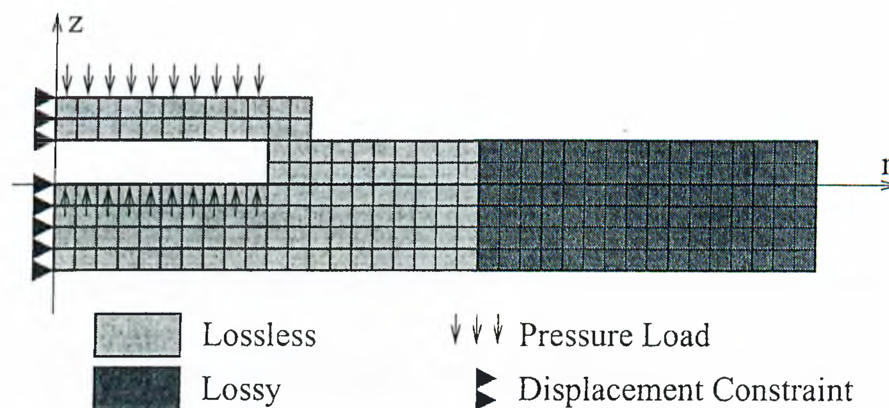

Figure 7.2: Finite-element model of the cMUT.

be kept small to minimize the impedance mismatch at the boundary of the lossless and lossy regions. On the other hand, the lossy region should provide enough attenuation so that incident waves at the model boundary should be well attenuated and the reflected waves at that end should not result in a significant standing wave pattern. This can be achieved by having a very long attenuating region as compared to the largest wavelength.

The structure of Fig. 7.2 is used to run harmonic analyses using ANSYS 5.5 [1] to test the validity of our method. The indicated pressure loads are applied together with the displacement constraints. ANSYS enables the use of an axisymmetric model, therefore we were able to model the cMUT as the 2-D structure of Fig. 7.2. As a first check, we look at the particle displacement at the surface of the substrate as a function of radial

[1]©SAS IP, Inc.

distance. Displacement is expected to decay monotonically with $\sqrt{r}$ [38]. Fig. 7.3 shows a plot of nodal displacement magnitude as a function of radial distance at excitation frequencies 1.0 MHz. (left) and 3.0 MHz. (right). The radial distances up to 30mm

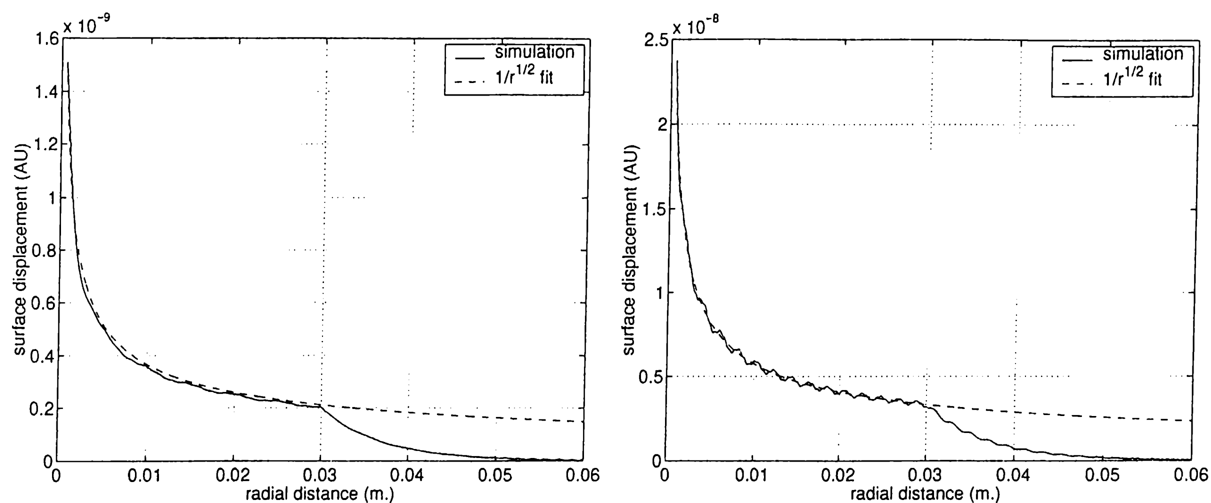

Figure 7.3: Magnitude of nodal displacement on substrate (Left 1.0, Right 3.0 Mhz).

are in the lossless region of the model and, as expected, there is a good agreement between the magnitude and the $1/\sqrt{r}$ curve shown with the dashed line. For radial distances from 30 mm. to 60 mm. wave magnitude dies away and, as the plot has reasonable smoothness, there is no significant reflection at either boundary. As the attenuation encountered by the radial wave modes was a function of frequency, the attenuation constants used in the simulations had to be adjusted for each frequency step to get the above results. In order to run harmonic analyses conveniently for a large range of frequencies (without the need to adjust attenuation for each frequency step), a general expression for the attenuation parameter of the analysis was developed. Fig. 7.4 shows how a general expression was found for the ANSYS dump parameter by fitting an analytically obtained curve to the attenuation values determined by trial-and-error (i.e., running simulations for each frequency step to have reasonable reflection at model boundaries). The expression for the analytic material dumping constant C curve turns out to have the form $C = C_0/f^2$ with C_0 being a constant and f the frequency.

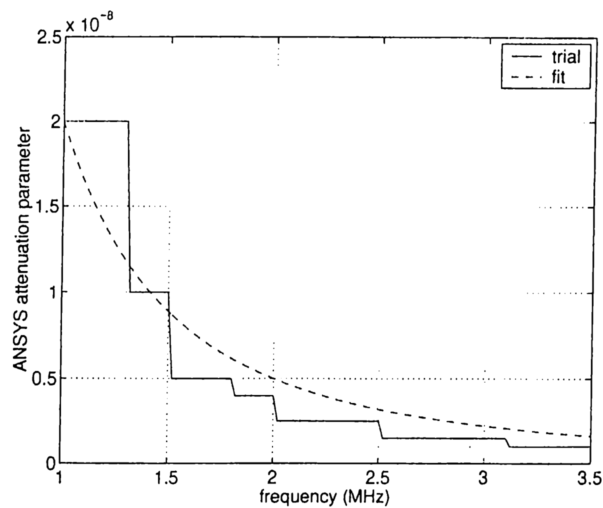

Figure 7.4: Fitted curve on ANSYS damp parameter determined by trial-and-error.

7.2 Acoustic Impedance of cMUT with Loss

Fig. 7.5 shows a typical simulation result for a cMUT with substrate loss. The device

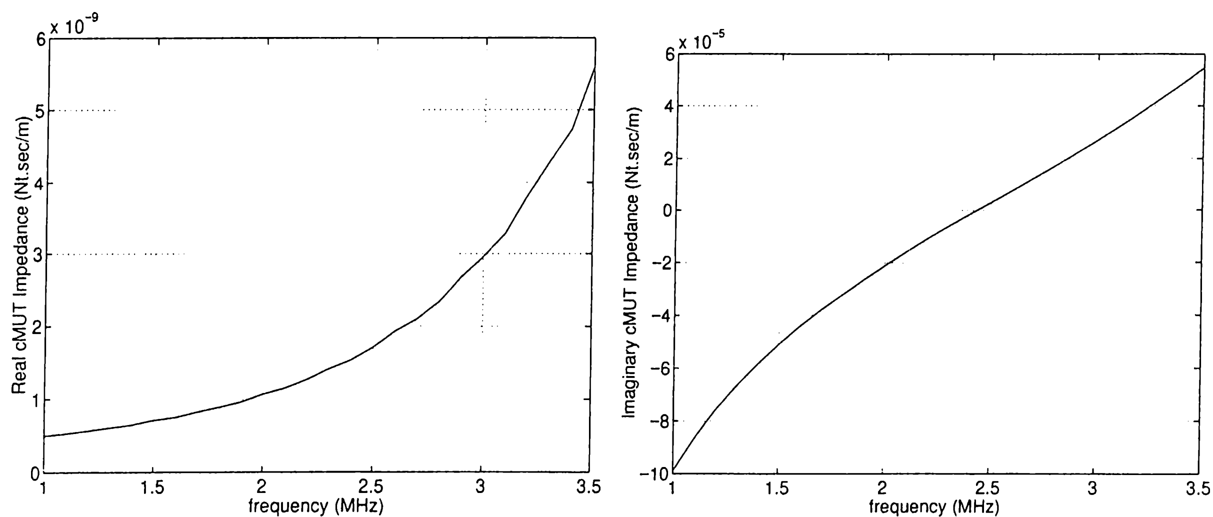

Figure 7.5: Impedance of cMUT with substrate loss (real and imaginary parts)

dimensions used in the simulations are around 1/10 of the wavelengths of plate modes present in the substrate [39], therefore they are expected to show the characteristics of point sources, for which the real impedance is a decreasing function of frequency. The

real impedance for a point contact is depicted in Fig. 7.6. However, the real part of

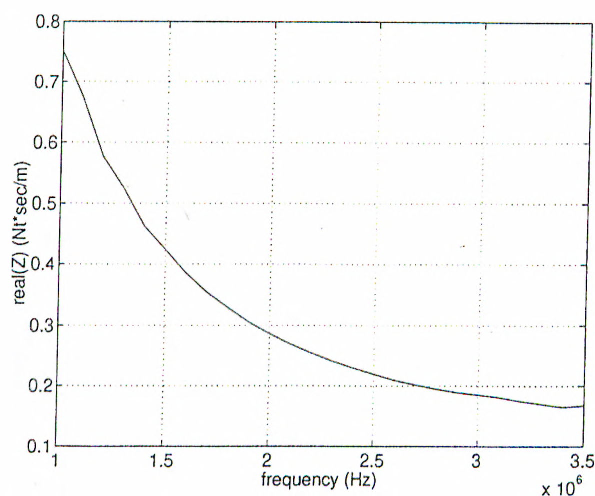

Figure 7.6: Real impedance for a point contact.

the membrane impedance found from the simulations exhibits a completely unexpected behavior: the impedance increases with frequency. To justify our simulation results, we divide the model into two parts, for which the individual results can be verified by comparing them with analytic quantities. Then, we combine the two analysis results to see whether they reveal the original simulation outcome.

The first subdivision of the EM model consists of the substrate alone. We remove the membrane from the model, and apply a force to the nodes which were in touch with the rim of the membrane (Fig.7.7). The simulation yields the nodal velocity values at

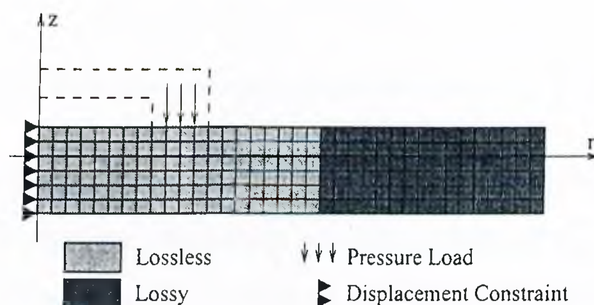

Figure 7.7: Submodeling I : Substrate impedance.

the excitation point, and those are used to compute the substrate impedance for circular

excitation. The measured substrate impedance Z_{sub} has a real part depicted in Fig 7.8. As expected from the case of point excitation, we get a curve decreasing with frequency.

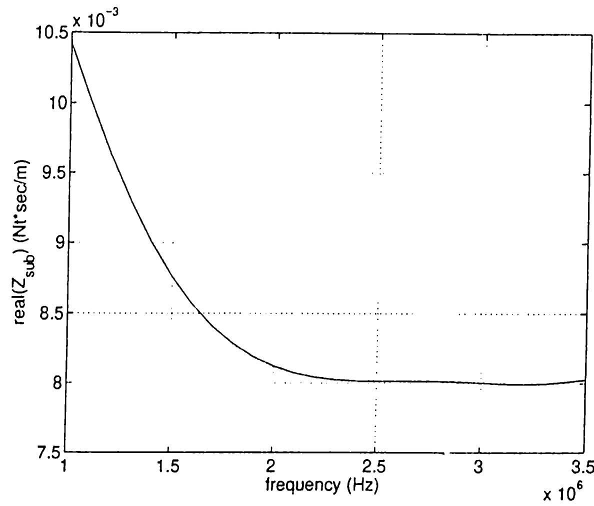

Figure 7.8: Real substrate impedance for circular excitation.

The second part of the analysis, drops out the substrate, and finds a two-port representation for the cMUT membrane, with the ports being the center of the membrane (where electro-static forces are applied) and the membrane rim (Fig.7.9). Device parame-

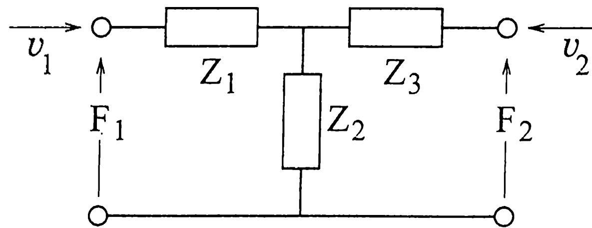

Figure 7.9: Two-port representation for the cMUT membrane.

ters Z_1, Z_2 and Z_3 are found by running simulations on the clamped membrane (Fig.7.10). Clamping nodes at the rim is equivalent to setting v_2 of Fig. 7.9 to zero, or equivalently, making Port-2 *open.* Measuring the velocity at the excitation point yields Z_{in}, the input impedance at Port-1. Meanwhile, we record the reactive force at the clamped nodes, which is F_2. These two reveal values of Z_1 and Z_2. To find Z_3 we run another simulation

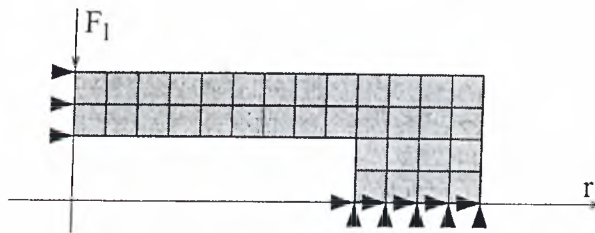

Figure 7.10: Submodeling II : Membrane as a two-port.

to find Z_{in} when nodes at the rim are set free to move, i.e., Port-2 is *shorted*. Hence,

$$Z_1 = Z_{in,open}(1 - F_{2,open})$$
$$Z_2 = Z_{in,open}\, F_{2,open}$$

and we can solve for Z_3 from

$$Z_{in,short} = Z_1 + Z_2 // Z_3$$

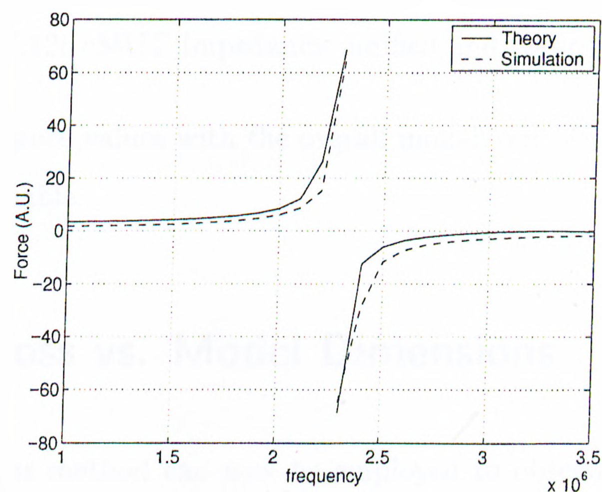

Figure 7.11: Forces at the rim of the membrane.

The simulation results for the membrane are in complete agreement with Mason's model [14] as depicted in Fig.7.11 where theoretical and simulated values for the force on the membrane rim are shown.

The membrane impedance Z_{mem} can, then, be found by combining the results of the

two analyses, i.e.,

$$Z_{mem} = Z_1 + Z2//(Z_3 + Z_{sub}) \tag{7.1}$$

Fig.7.12 shows the membrane impedance from the original model together with the combined result of the two independent analyses. The results of the combined analysis

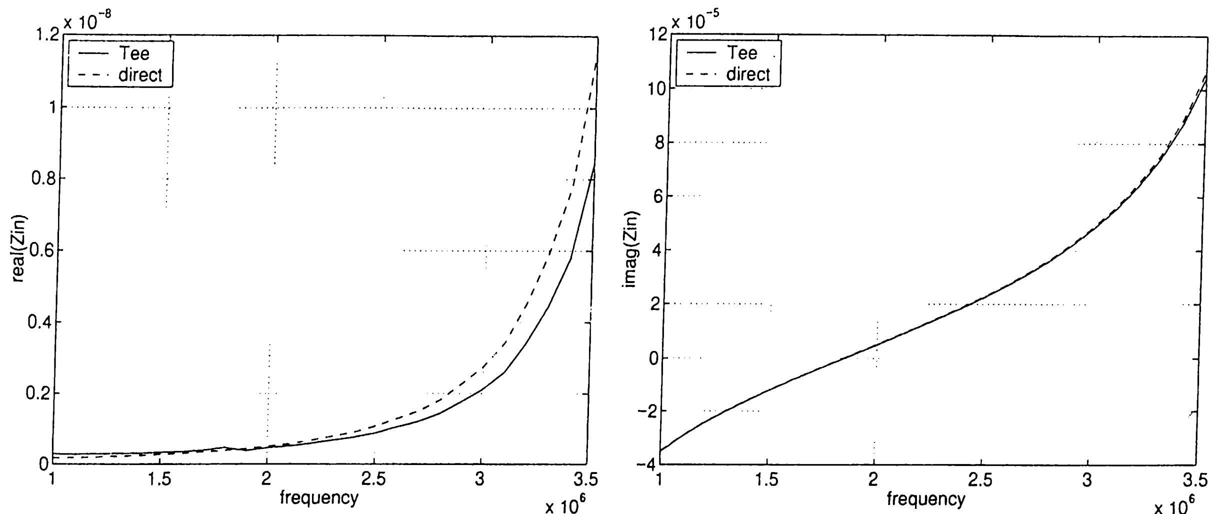

Figure 7.12: cMUT Impedance: unified and two-part models

yield the same impedance values with the overall model, out of which we conclude that the FEM data are reliable.

7.3 cMUT Loss vs. Model Dimensions

The developed analysis method can now be employed to observe the effects of model dimensions on the cMUT impedance. Here, we discuss two of them: substrate thickness, and the rim width (parameters t_s and w of Fig.7.1, respectively).

Simulations for various substrate thicknesses revealed that the real part of the cMUT impedance increases with decreasing substrate thickness (viz. Fig.7.13). This is a reasonable result, as one might say that the thinner the substrate, the easier it can be vibrated. As the dimensions and driving forces of the cMUT itself do not change, we might expect

that more power goes into plate modes that the substrate supports. On the other hand, the rim width w did not have a significant effect on the cMUT impedance, seen from the simulation results.

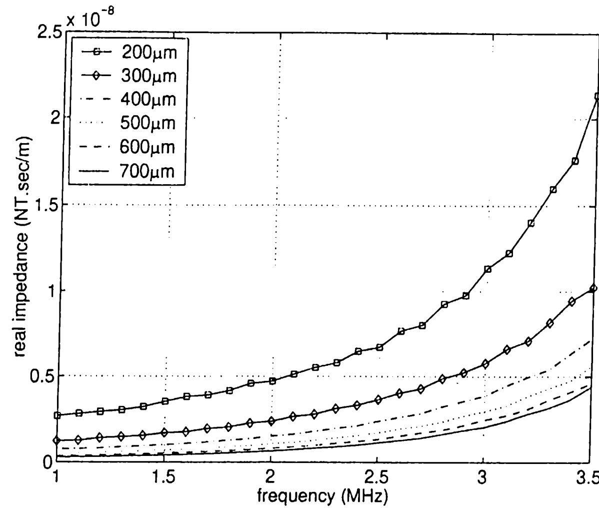

Figure 7.13: Real part of cMUT impedance for various substrate thicknesses.

7.4 Normal Mode Theory Analysis

The power coupled into the cMUT substrate goes into the plate modes (*Lamé waves*) [39] supported by the silicon wafer over which the device is constructed. Analytic formulation

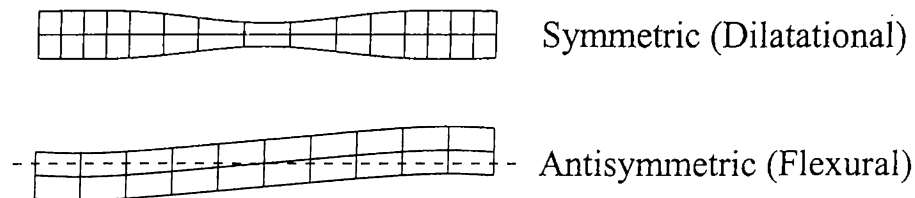

Figure 7.14: Lowest (0th) order symmetric and antisymmetric plate modes (S0 and A0).

of the wave equation reveals that the supported orthogonal wave modes divide into two groups, namely, symmetric and antisymmetric. Fig.7.14 shows two of the lowest plate modes. The names symmetric and antisymmetric reflect the nature of particle

displacement: for the former, displacements are symmetric with respect to a central plate midway to the wafer's two surfaces. The latter, on the other hand, is also named as flexural because of the antisymmetric characteristics of particle motion.

The motivation behind a "Normal Mode Theory Analysis" is to determine the power that goes to each individual wave mode. This can be consequently used to analytically evaluate the loss impedance of a cMUT device of particular dimensions. Here we present the decomposition of plate waves into their orthogonal modes, and show some FEM simulation results.

The *Rayleigh-Lamb frequency equations* relate the propagation constant β of a particular wave mode to the transverse wave vector components k_{tl} and k_{ts}. We have

$$\frac{\tan k_{ts}b/2}{\tan k_{tl}b/2} = -\frac{4\beta^2 k_{tl}k_{ts}}{(k_{ts}^2 - \beta^2)^2} \tag{7.2}$$

for the symmetric solutions, and

$$\frac{\tan k_{ts}b/2}{\tan k_{tl}b/2} = -\frac{(k_{ts}^2 - \beta^2)^2}{4\beta^2 k_{tl}k_{ts}} \tag{7.3}$$

for the antisymmetric solutions, where b is the plate (substrate) thickness. Combining Eq.'s 7.2 and 7.3 with the expressions relating k_{tl}, k_{ts}, β and ω, the radial frequency, i.e.,

$$k_{tl}^2 = \left(\frac{\omega}{V_l}\right)^2 - \beta^2, \qquad k_{ts}^2 = \left(\frac{\omega}{V_s}\right)^2 - \beta^2, \tag{7.4}$$

we get the dispersion relations for the modes supported by the substrate of interest. Here, V_l and V_s are the longitudinal and shear wave velocities for the substrate material. Fig.7.15 shows the dispersion curves found for a 500 μm thick silicon wafer. For the frequency range of interest, the only supported wave modes are the lowest order symmetric and antisymmetric modes, or S0 and A0, respectively.

The next step in the analysis involves the determination of the power that couples into each individual wave mode. An arbitrary distribution of particle velocity $\mathbf{v}(x, z)$ and associated stress field $\mathbf{T}(x, z)$ along the thickness of the plate can be written as

$$\mathbf{v}(x, z) = \sum_{n=0}^{\infty} a_n(x)\mathbf{v}_n(z) \tag{7.5}$$

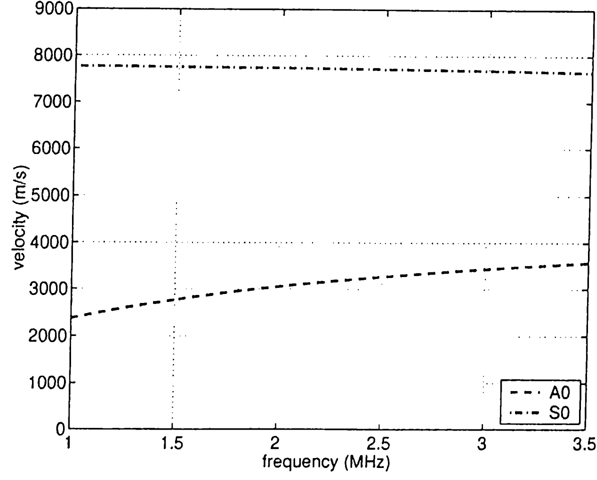

Figure 7.15: Dispersion curves for A0 and S0 modes in the frequency range 1.0–3.0 MHz

$$\mathbf{T}(x,z) = \sum_{n=0}^{\infty} a_n(x)\mathbf{T}_n(z) \cdot \mathbf{x} \tag{7.6}$$

where the orthogonal field distributions $\mathbf{v}_n(z)$ and $\mathbf{T}_n(z) \cdot \mathbf{x}$ are in fact the field distributions of the propagating Lamb waves in the free silicon plate. The solution of the boundary value problem to determine expressions for the supported wave modes reveal that particle velocities along the thickness are

$$v_x = \mp i\beta \left[\cos k_{tl}z \ \cos k_{ts}b/2 - \frac{\beta^2 - k_{ts}^2}{2\beta^2} \cos k_{tl}b/2 \ \cos k_{ts}z\right] e^{\mp i\beta x} \tag{7.7}$$

$$v_z = \mp i\beta \left[-k_{tl} \sin k_{tl}z \ \cos k_{ts}b/2 - \frac{\beta^2 - k_{ts}^2}{2k_{ts}} \cos k_{tl}b/2 \ \sin k_{ts}z\right] e^{\mp i\beta x} \tag{7.8}$$

for symmetric modes, and

$$v_x = \mp i\beta \left[\sin k_{tl}z \ \sin k_{ts}b/2 + \frac{\beta^2 - k_{ts}^2}{2\beta^2} \sin k_{tl}b/2 \ \sin k_{ts}z\right] e^{\mp i\beta x} \tag{7.9}$$

$$v_z = \mp i\beta \left[-k_{tl} \sin k_{tl}z \ \cos k_{ts}b/2 - \frac{\beta^2 - k_{ts}^2}{2k_{ts}} \cos k_{tl}b/2 \ \sin k_{ts}z\right] e^{\mp i\beta x} \tag{7.10}$$

for antisymmetric modes. The mode amplitude a_n can be found by substituting the corresponding orthogonal mode expansions for the arbitrary fields in Eq. 7.5 and 7.6 in the orthogonality relation

$$a_n = \frac{1}{4\mathrm{P}_{nn}} \int_{-t_s}^{0} (-\mathbf{v}_n^*(z) \cdot \mathbf{T}(z) - \mathbf{v}(z) \cdot \mathbf{T}_n^*(z)) \cdot \mathbf{x} \ dz. \tag{7.11}$$

P_{nn} is the average power flow of the mode per unit width in the x-direction for $a_n = 1$. To apply this methodology to the circularly symmetric geometry, it is inherently assumed that the calculations are performed at a radius which is sufficiently far away from the membrane.

The total power radiated, hence dissipated by the lossy region, P_{tot} can be found by

$$P_{tot} = 2\pi r_1 \frac{1}{2} Re\left\{\int_{-t_s}^{0} \left(v_x^* T_{xx} + v_z^* T_{xz}\right) dz\right\} \tag{7.12}$$

where all stress and velocity values are at a cross section at $r = r_1$, with r_1 being inside the lossless part of the model and close to the boundary of the lossy and lossless regions. The radiated power levels of the Lamb wave modes are then found by substituting the results of the finite element analysis in Eq. 7.11 and using the relation $P_n = 2\pi r_1 |a_n|^2 P_{nn}$.

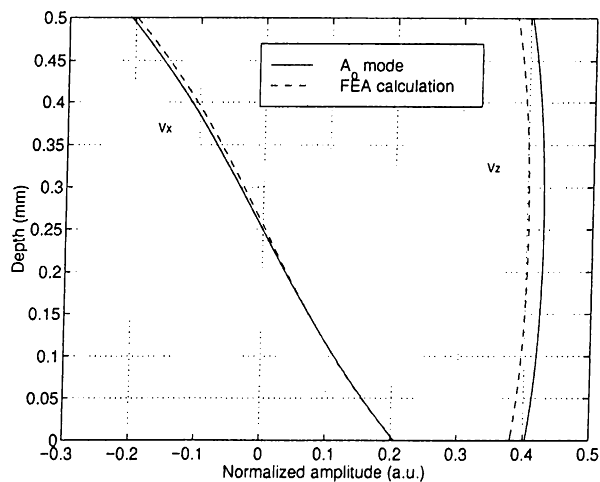

Figure 7.16: Particle velocity field distribution (A_0 and FEA) at 1 MHz (r_1=29.9 mm).

The modal decomposition results show that the A_0 mode Lamb wave is the dominant source of the radiation loss, especially at lower frequencies. This can be clearly seen in Fig. 7.16 where the modal particle velocity field distribution of the A_0 mode and the result of the FEA calculation at 1 MHz are plotted. The antisymmetric nature of the radiated field is very similar to the A_0 mode. Radiated power calculation results support this conclusion. The total radiated power loss as a function of frequency is plotted in

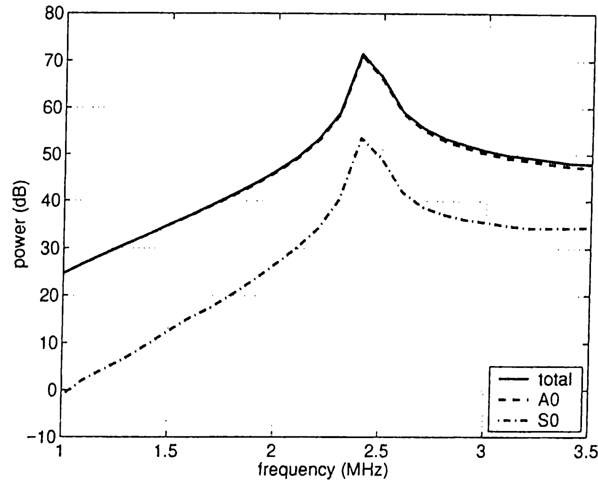

Figure 7.17: Total power coupled to the substrate and powers for A_0 and S_0 modes.

Fig. 7.17 as the solid line. As expected, the radiated power is maximum at the resonance frequency.The power radiated by the A_0 and S_0 modes are also depicted in the same figure. It is evident that the A_0 mode carries nearly 100% of the total radiated power, whereas the S_0 mode is becomes a more important source of loss at higher frequencies. These results enable us to derive an equivalent circuit model of the membrane with physically based loss terms as described below.

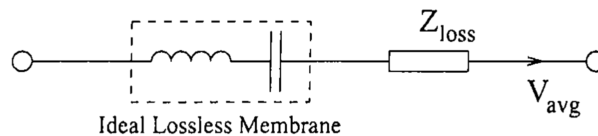

Figure 7.18: Equivalent circuit model which includes cMUT substrate loss.

Equivalent Circuit Model

The ideal lossless membrane is modeled as a capacitor and an inductor in series representing its compliance and mass, respectively. Substrate loss can be included to the model as a series frequency dependent resistor (Fig. 7.18). The value of this resistor can be found by finding the acoustic impedance Z_a of the membrane from FEM results: If the applied pressure on element faces is P, the the total force on the membrane surface

is $F_{tot} = \pi a^2 P$. The average velocity of the membrane, V_{avg} is given by

$$V_{avg} = j\omega \frac{1}{\pi a^2} \int_0^a 2\pi r \, u(r) \, dr \qquad (7.13)$$

where $u(r)$ is the membrane displacement found from the FEM analysis. The acoustic impedance of the membrane is, then, given by $Z_a = F_{tot}/V_{avg}$. As we claim that the real part of Z_a accounts for the substrate loss, the resistance found by computing the power propagating out from the membrane, should be identical to $Re(Z_a)$. The loss resistance is then given by $0.5 P_{tot}/|V_{avg}|^2$, where P_{tot} is calculated using Eq. 7.12. Fig. 7.19 shows that

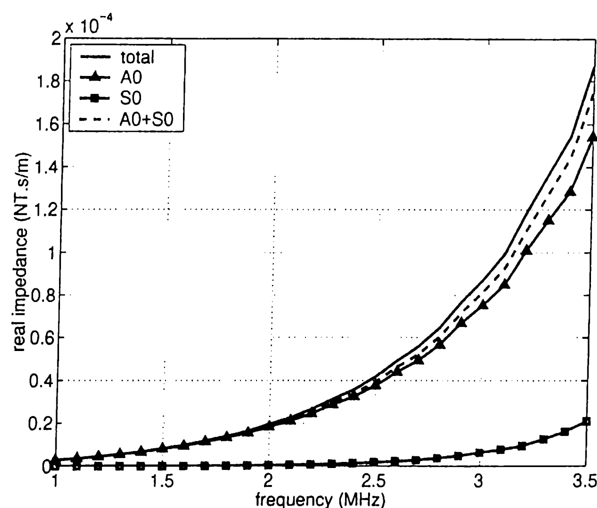

Figure 7.19: Total loss resistance of cMUT and resistances of A_0 and S_0 modes.

the real part of the membrane impedances computed using the two suggested methods are indeed in agreement. The value of loss resistance is about 1/100 of the impedance of air as the loading medium, hence, power loss will be −20dB with respect to the radiated power of an air transducer.

The loss resistance can be further divided into terms each representing the loss due to a different propagating mode in the silicon substrate giving more insight into the physical loss mechanism. The result of this calculation for the A_0 and S_0 modes are also depicted in Fig. 7.19. This results suggests a revised model for the membrane with substrate loss: Loss term associated with each possible wave mode appear as distinct

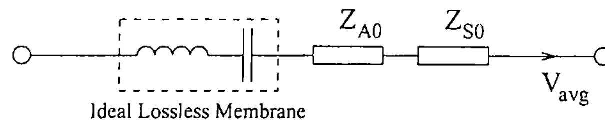

Figure 7.20: Equivalent circuit model revisited: modal loss accounts for total loss.

loss components in the equivalent circuit, as depicted in Fig. 7.20. The analysis can be extended to a generalized model that includes components with analytically computed values, which requires the knowledge of the surface impedance of each mode, so that the loss computation method described in Sec. 7.2 can be employed.

Chapter 8

DEVICE FABRICATION

Micromachining, or the "art" of micron-sized mechanical structures is a natural consequence of silicon processing techniques mainly intended for the production of integrated circuits. We will start out with a brief introduction on micromachining terminology, and this will be followed by the fabrication method that we have developed at the "Advanced Research Laboratories" (ARL) of the the Physics Department of Bilkent University. Measurement results will be presented at the end of this chapter.

8.1 An Introduction to Microfabrication

Each step of a micromachining process involves the following substeps:

1. Deposition of a certain layer, either metal or a silicon compound.
2. Patterning of a certain structure using lithography.
3. Removal of the unwanted regions using either wet or dry etch.

A quartz plate of size 10×10 cm^2 bearing the shapes to be carved on the structure is used as a mask in the lithography step. After depositing the material of choice, the sample is coated with a light-sensitive paint known as the photoresist. The mask is then

placed on the sample and the sample is exposed to light. This transfers the structure on the mask to the photoresist, and the exposed parts are chemically altered so that they are "washed-away" by the developer, a chemical that attacks exposed photoresist. At this stage the regions of the deposited layer that we want to keep are protected by a photoresist film. Etching, or the process of exposing the sample either to a chemical or a mechanical corrosive able to act upon it, removes the uncovered regions of the layer, but, does not have an effect on the photoresist and, consequently the sample under it. Thus, at the end of etching, the deposited layer is patterned. Consecutive application of the above procedure eventually results in the desired micro-structure. App.A presents a small glossary of micromachining terms.

8.2 cMUT Fabrication

cMUT devices were fabricated at ARL using standard deposition, lithography and wet/dry etch techniques. The following set of equipment were involved in the fabrication carried out in the Class-100 Clean Room:

Equipment	Vendor and Type
Conventional Lithography	Karl-Suss MJB3
Plasma Deposition (PECVD)	PlasmaLab 8510C
Reactive Ion-Etching	Leybold LE-301
Metalization	Leybold LE-560
Bonding	Westbond 7400 A

Table 8.1: Equipment used in cMUT fabrication

The fabrication involves a 3-mask process whose steps are described below:

STEP#1 : Cleaning

Cleaved doped silicon samples of size 12×12 mm^2 are first cleaned using three solvents,

namely TCA (trichloro-ethane), ACE (acetone) and ISO (iso-propyl alcohol). Table 8.2 lists the time durations for each individual chemical bath and the temperature setting. The sample is then rinsed thoroughly under continuously flowing DI water for about a

Solvent	Duration	Temperature
TCA (tri-chloro ethane)	2 min.	BOILING
ACE (acetone)	5 min.	ROOM (21°C)
ISO (iso-propyl alcohol)	2 min.	BOILING

Table 8.2: Chemicals used in sample cleaning

couple of minutes, and dried using a N_2 gun. To assure complete dryness before further processing, the sample is held on a 120°C hot-plate for 2 minutes.

STEP#2 : Sacrificial Layer Deposition & Patterning

The first lithography step of the process involves the deposition and patterning of the sacrificial layer, which will determine the membrane shape and air-gap thickness. After numerous trials, the most vulnerable material to HF (hydrofluoric acid) was found to be Silicon-rich Nitride (Si_xN_y). A layer of 5000Å thick Nitride is deposited onto the silicon substrate. The following lithography step patterns the hexagonal shaped membranes. RIE (Reactive Ion Etch) is employed to etch away the non-active regions of the membrane. Tri-solvent cleaning is applied again before the next deposition step.

STEP#3 : Membrane Deposition

Tests to find two materials which have significant difference between their HF etch times revealed that amorphous Silicon (a-Si) was almost insensitive to HF when compared to Si_xN_y, the sacrificial layer material. This was necessary to be able to etch away the sacrificial layer without any harm to the membrane itself, and is termed as "selective etch". Having chosen the membrane material, we coat the sample with a-Si and bury the already-patterned sacrificial layer under this new layer.

STEP#4: Metalization (Electrode Deposition)

Before we go to the underetch of the sacrificial layer, we deposit the top electrode utilizing a metalization process. The metalization does not cover the whole membrane, but is a small area at the center of the membrane due to bandwidth optimization criteria [40]. The so-called "image-reversal" technique is applied for metalization because it provides a better profile of the photoresist edges that make the lift-off much easier. The metalization pattern is provided by a positive mask. After lithography, the sample is placed on a 120°C hot-plate for 2 minutes. Then, a blank exposure of uV light is made. This "reverses" the chemical properties of the photoresist, so that the initially exposed regions of resist become defiant towards the developer. Then, the whole sample is coated with a 3000Å thick gold layer. The regions determined by the mask get covered with the gold layer, while resist blocks gold to reach the sample at regions to remain uncovered. During lift-off, acetone removes remaining resist together with the gold layer on top of it.

STEP#5: Underetch

The last step of the process involves the removal of the sacrificial layer that still remains buried under the membrane. Another lithography step is involved to "drill." 2 μm wide holes at the corners of the hexagonal membrane structure defined by the sacrificial layer. The etchant used for the underetch is 1:40 HF:H_2O made from a 50% HF solution, and the etch time is about 10 minutes.

Figures 8.1, 8.2 and 8.3 provide a pictorial representation of the fabrication, while in Fig. 8.4 we depict the top view of the sample for various intermediate steps of the fabrication. Tables 8.3 and 8.4, on the other hand, are process charts showing useful timing and set-up information for the particular instruments used in the Advanced Research Laboratories.

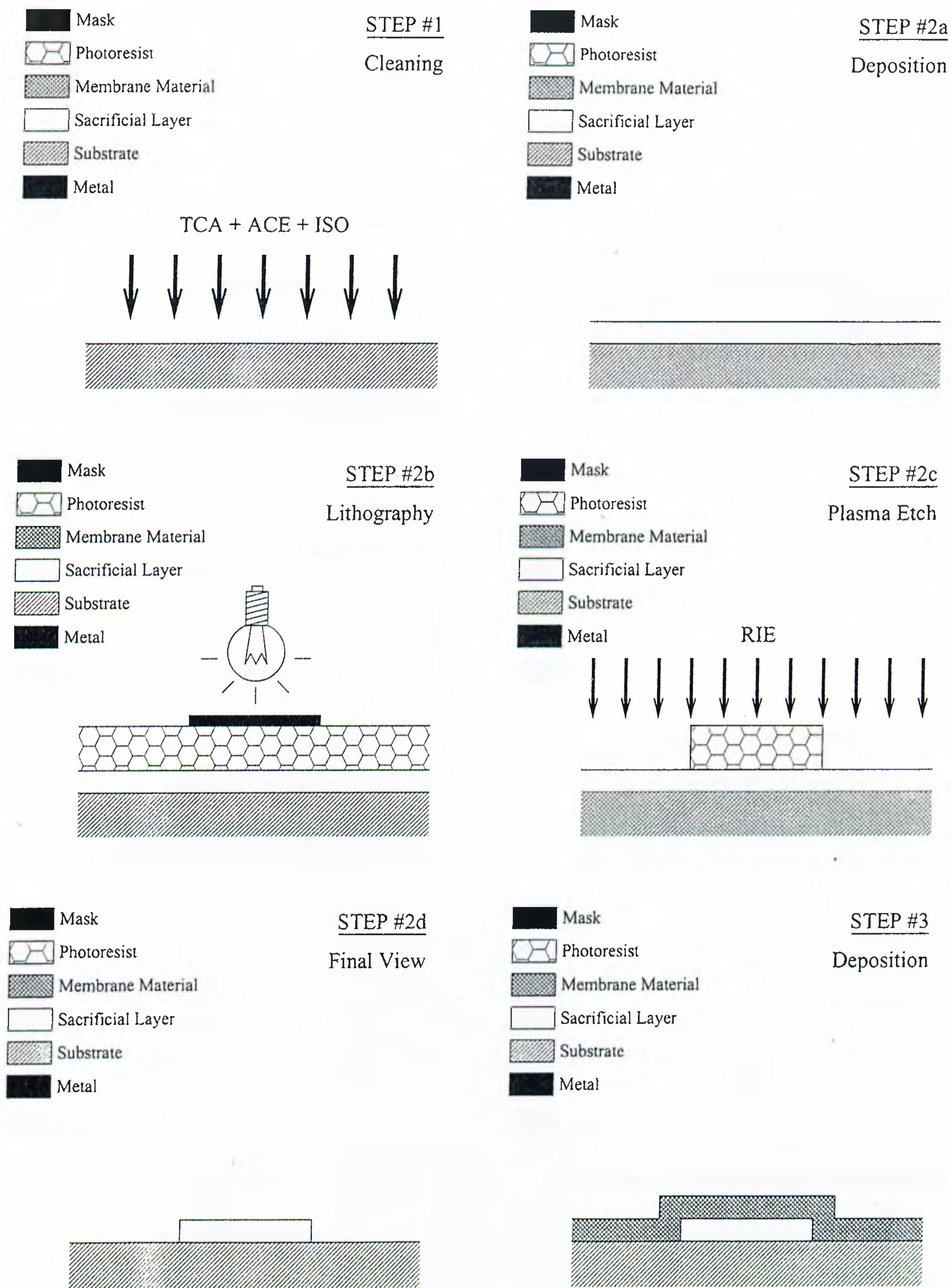

Figure 8.1: Process steps 1, 2a, 2b, 2c, 2d and 3.

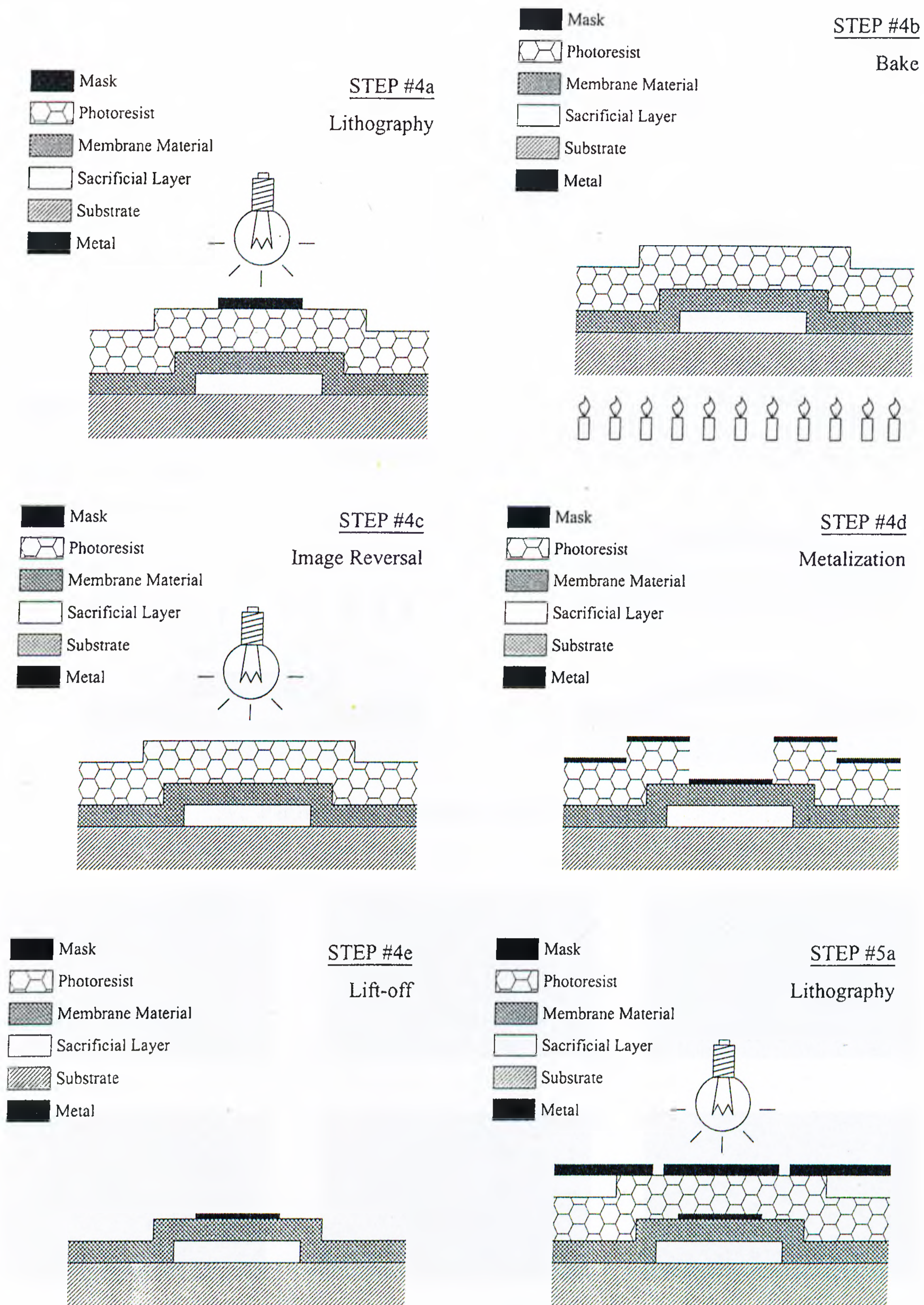

Figure 8.2: Process steps 4a, 4b, 4c, 4d, 4e and 5a.

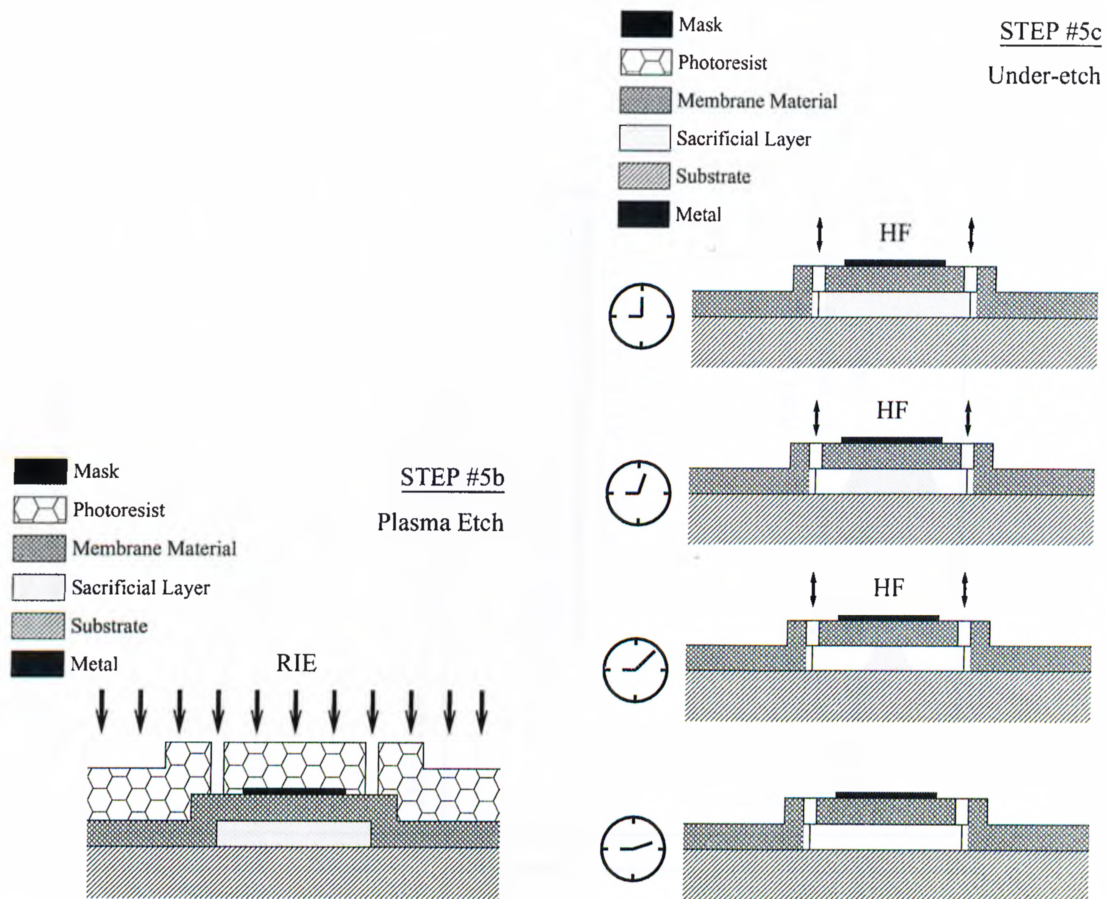

Figure 8.3: Process steps 5b and 5c.

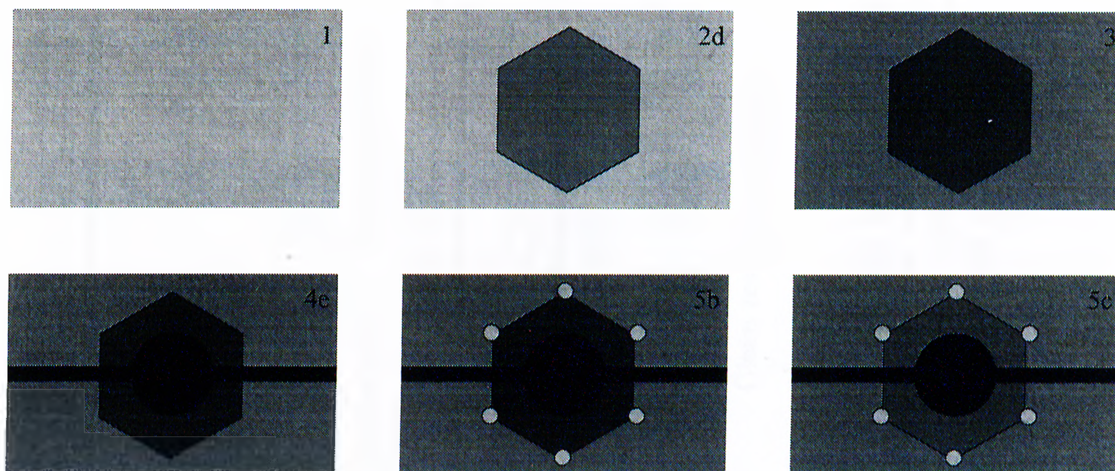

Figure 8.4: Top view of cMUT structure for various fabrication steps.

Chart #1: Sacrificial Deposition

Cleave Samples
TCA + ACE + ISO
PECVD

Layer Type	: SiN_x Silicon Nitride
PECVD Process File	: **SIN1C**
Duration & Temperature	: 63 min. @ 250°C
Final Layer Thickness	: ~ 5000 Å

Chart #2: Sacrificial Patterning

TCA + ACE + ISO
Spin @ 4000 RMP
Pre-bake 55 sec. @ 110°C

Edge-beat	Expose	20 sec @ 8.0 mW	Develop ~ 1 min.
Patterns	Expose	20 sec @ 8.0 mW	Develop ~ 50 sec.

Hard-bake 2 min. @ 120°C

Developer : 20 ml. / 80 ml. AZ400/H_2O

Chart #3: Sacrificial Etch

RIE

Plasma Etch (RIE)	1 min.	O_2	20 sccm @ 51 Watt
	15 min.	CCl_2F_2	20 sccm @ 99 Watt

Clean resist with **ACE**

Notes:

1. The CCl_2F_2 etch must not be shorter than 15 min. to prevent sacrificial remainder outside membrane area. Otherwise membrane material goes of during underetch.
2. Use a Q-tip when cleaning resist with ACE.

Chart #4: Membrane Deposition

TCA + ACE + ISO
PECVD

Layer Type	: a-Si Amorphous Silicon
PECVD Process File	: **ASI100A**
Duration & Temperature	: 40 min. @ 100°C
Final Layer Thickness	: ~ 5000 Å

Table 8.3: Process charts 1–4

Chart #5: Metal Patterning (Image Reversal)

TCA + ACE + ISO
Spin @ 4000 RPM
Pre-bake 55 sec. @ 110°C
Expose 6 sec. @ 8.0 mW.
Bake 2 min. @ 110°C (for image reversal)
Expose (blank) 20 sec. @ 8.0 mW.
Develop ~ 1 min. 15 sec.

Developer : 20 ml. / 80 ml. AZ400/H_2O

Chart #6: Metal Deposition & Lift-off

Box-Coater
Lift-off

Coater Settings	0.060 kÅ Ti
	1.000 kÅ Au

Notes:

1. Box-coater deposits about ×4 of its settings.
2. Cut about 0.5 gr. gold. A thin line of Ti powder will do.
3. Use plenty of ACE in lift-off holder.

Chart #7: Hole Patterning

TCA + ACE + ISO
Spin @ 5000 RPM

Edge-beat removal	Expose 20 sec. @ 8.0 mW.
	Develop 50 sec. to 1 min.
Holes	Expose 20 sec. @ 8.0 mW.
	Develop 1 min. 20 sec. +
	Hard-bake 2 min. @ 120°C

Chart #8: Hole Etch & Sacrificial Underetch

RIE

Plasma Etch (RIE)	1 min.	O_2	20 sccm @ 51 Watt
	15 min.	CCl_2F_2	20 sccm @ 99 Watt

Underetch ~ 10min. in 1/40 HF/H_2O
Clean resist with ACE + Q-tip
Dry 2 min. @ 120 oC

Notes:

1. Do not remove resist before underetch.

Table 8.4: Process charts 5–8

8.3 Device Dimensions

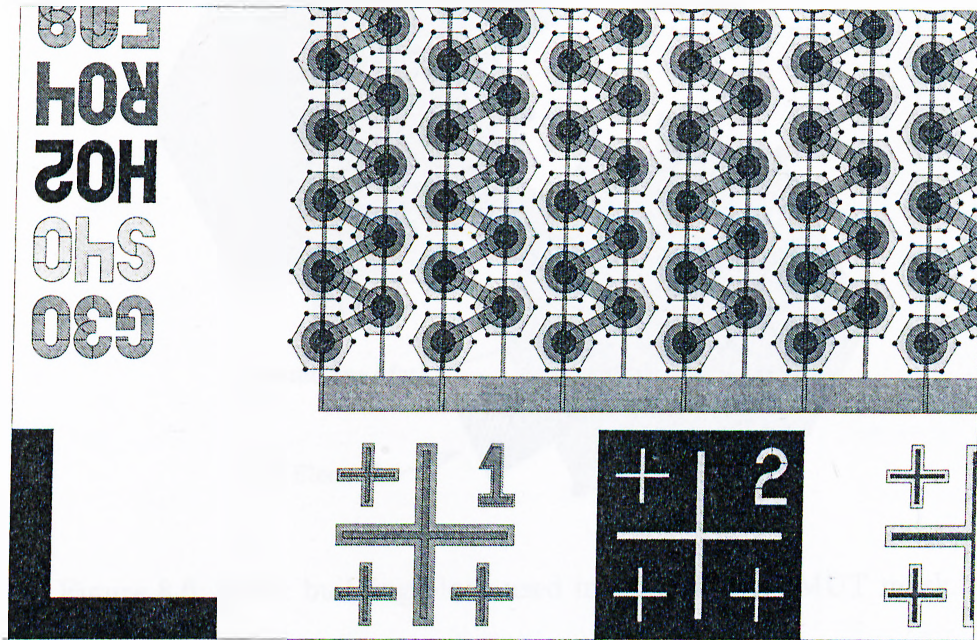

Figure 8.5: Zoomed view of mask (active membrane area 500×250 μm^2 approx.).

Fig. 8.5 shows part of the mask used in device fabrication with all layers overlapped on a single figure. Active membrane area is to the upper right corner of the figure while features on the sides are alignment marks, corner marks, and information marks on structure dimensions. Fig. 8.6 shows the basic building block used in the drawing of the cMUT mask. The hexagonal membrane mask determines the shape of the air gap. Holes are centered to the corner of the membrane, which are used during the underetch phase of the process. The membrane electrode is placed to the center of the hexagonal structure, and is tied to the next electrode with an additional stripe of metal. The GND electrode layer can be used to construct cMUT structures on an insulating substrate. The use of the GND electrode can further decrease the input capacitance of the device as the stripes interconnecting the membrane electrodes will not be on a grounded conducting substrate. On the complete mask, GND and membrane electrodes are combined at pads at the two opposite sides of the substrate to form bound points to the drive circuit.

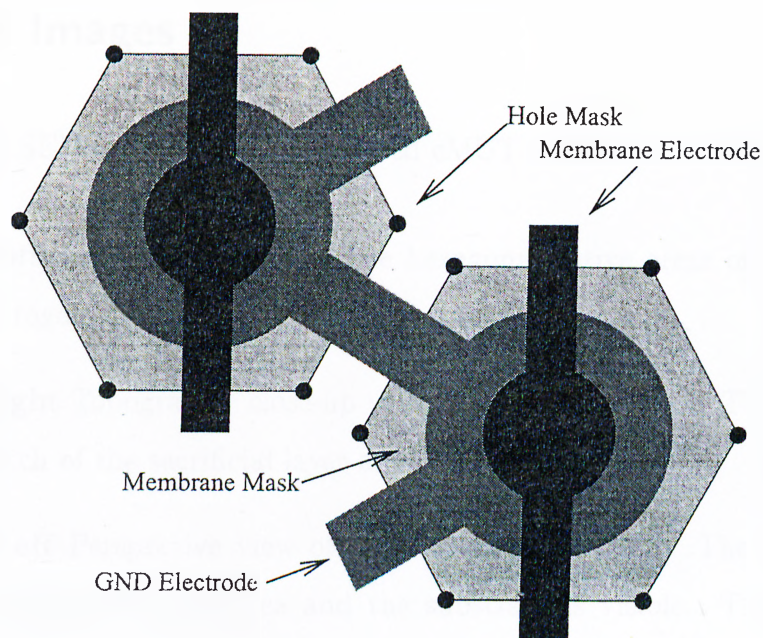

Figure 8.6: Basic building block used in drawing the cMUT mask.

The following is a list of fabrication parameters:

Parameter	Value
Center-to-center membrane distance	: 50 μm
Membrane radius	: 40 μm
Nitride thickness	: 5000 Å
Air-gap thickness	: 5000 Å
Au Metalization Thickness	: 3000 Å
Metalization radius	: 8, 16, 24 μm
Total number of active cells	: 3×8000
Substrate thickness	: 500 μm

Table 8.5: cMUT fabrication process parameters.

The fabricated devices rest on a doped conducting silicon substrate, therefore the GND electrode mask was not used. The samples are, then, manually bonded to a copper PCB for testing purposes.

8.4 SEM Images

Fig. 8.7 shows 6 SEM images of the fabricated cMUT devices:

- **Upper Left** Top view of cMUT. The hexagonal active areas of the membranes are visible together with the circularly shaped top electrode.
- **Upper Right** Topographic close-up view of single cMUT cell. The holes used for the underetch of the sacrificial layer are clearly visible.
- **Central Left** Perspective view of a group of cMUT cells. The level difference between active membrane area and the substrate is visible. The Au electrode traces the level difference.
- **Central Right** Cross sectional view of single cMUT cell. This picture clearly shows the air gap between the membrane and the substrate.
- **Bottom Left** Cross sectional view of cMUT cell. In this picture complete cells interconnected with the sliced cell are also visible.
- **Bottom Right** Close-up view of cMUT cross-section. This picture shows the membrane profile at the membrane-substrate interface.

All pictures are taken using a JEOL Electron Microscope operated at 17 kV, located in the Advanced Research Laboratories (Class-100 clean-room) of the Physics Department of Bilkent University.

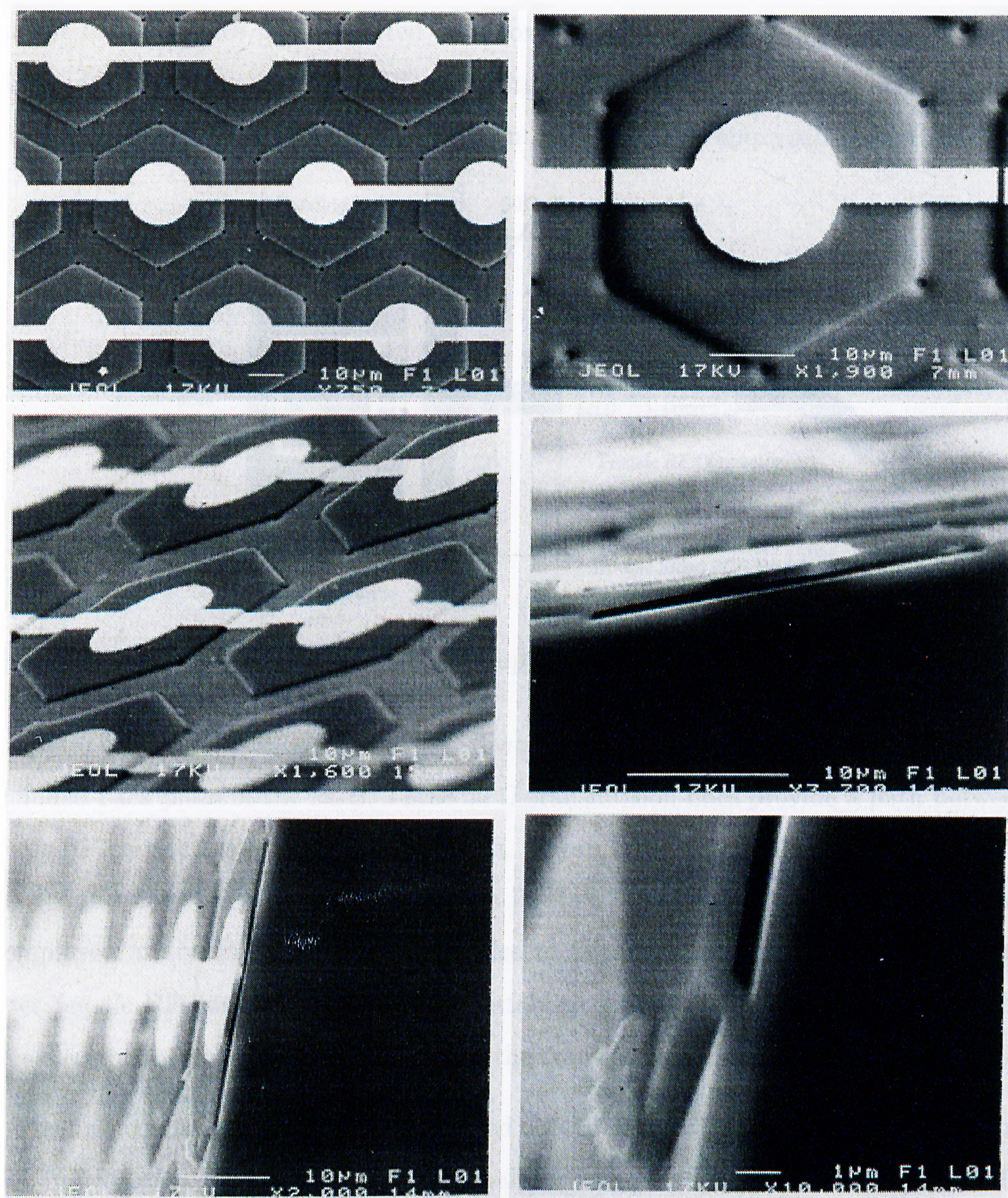

Figure 8.7: SEM images of fabricated cMUT devices.

8.5 Experimental Setup

As the cMUT device is constructed on a conducting silicon substrate, the back surface of the device can be used for GND connection. The device is mounted onto a double-sided PCB using silver epoxy, as shown in Fig. 8.8. The epoxy-silicon surface forms

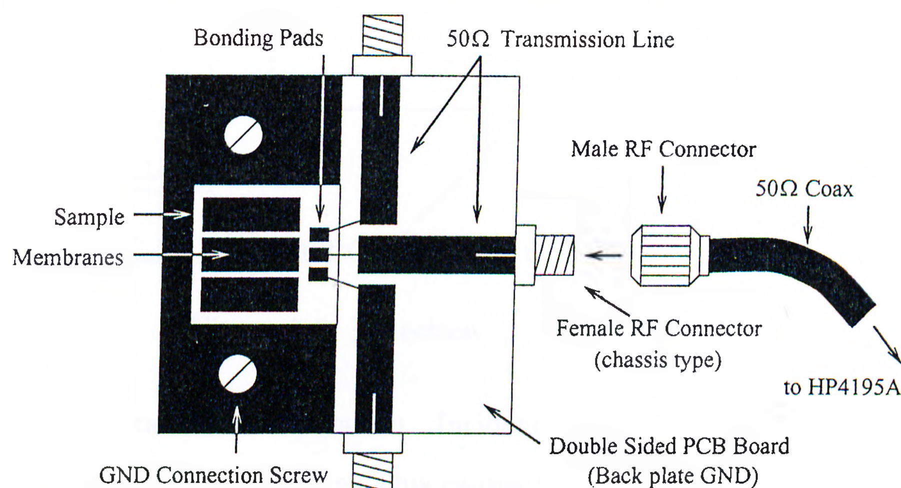

Figure 8.8: Experimental setup for cMUT characterization.

an ohmic contact of reasonable quality. Two screws connect the mount surface to the grounded back plate of the PCB. Three 50 Ω transmission lines provide a path between female RF connectors and the bonding pads. 30 μm thick Au bonding wires are used to make connections between the transmission lines and pads on the sample. Silver epoxy is employed at the PCB side of the Au wire to assure a mechanically strong contact. Three female RF connectors are used to establish individual connections between the three electrically isolated active regions on the transducer and the external electronics.

The first conducted test on the fabricated cMUT device was the measurement of the input impedance. A HP4195A Network Analyzer was connected to the setup shown in Fg. 8.8. Measurement results are provided in the following section.

As transducers were observed to be operational, a detection experiment set-up was

designed. The detection circuit employs a bias circuit followed by a low-noise transconductance amplifier [6, 41], as shown in Fig. 8.9. The RF-choke inductor provides the

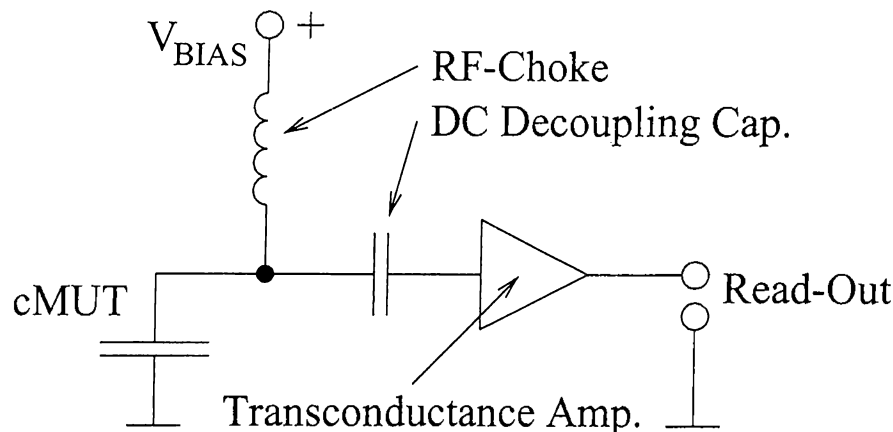

Figure 8.9: Detection circuit for cMUT.

necessary bias for transducer operation. Incident acoustic waves cause the membrane to vibrate, changing its capacitance. This causes an AC current to be generated by the transducer having the same frequency that of the acoustic excitation. The RF-choke is chosen to have a high enough value to block the generated AC current to leak into the DC supply. Having no other path, the transducer current flows into the transconductance amplifier, which outputs a voltage proportional to the input current, thus proportional to transducer displacement. Usually, the required inductor value for the choke is very large when the acoustic frequency range is considered. As realizing high-valued inductors requires bulky components, an inductive bias circuit is not quite suitable for devices with integrated electronics. This problem can be solved by employing resistive bias. The RF-choke is to be replaced by a resistor with value much larger than the input impedance of the amplifier. As the leak impedance of the cMUT itself is very large, it seems that an arbitrarily large resistor value can be chosen. However, a larger resistor value implies a larger amount of noise. Thus a compromise is to be made between output amplitude and noise.

The circuit model described in Fig. 8.10 is employed by the cMUT research group

at Ginzton Laboratory, Stanford University. The following rules apply for the choice of

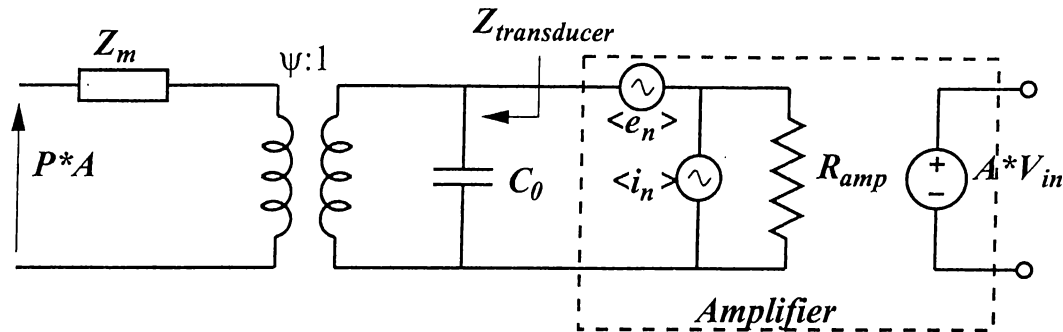

Figure 8.10: Ginzton detection circuit for cMUT. (courtesy Dr. Sanlı Ergun)

component values (by courtesy of Dr. Sanlı Ergun of Ginzton Laboratory):

- For air applications Z_m is a high-Q RLC circuit. For immersion applications Z_m is a low-Q RLC circuit. Therefore air applications are narrow band, immersion applications are wide band.

- It is possible to put an inductor between the amplifier and the transducer to eliminate the imaginary part of $Z_{transducer}$. However this makes the receiver circuitry resonant. For immersion applications it is something you do not want.

- The SNR at the output of the amplifier does not depend on the input impedance of the amplifier for it is the same impedance that the input referred noise sources of the amplifier see. Thus, making R_{amp} higher does not make SNR better, although it increases the signal level at the output.

- The SNR at the output is maximum when the impedance seen by the amplifier $|Z_{transducer}|$ is equal to $< e_n > / < i_n >$ ratio. You can put a transformer between the amplifier and the transducer to achieve this noise matching condition. You can have a wide-band transformer, but still it is something you cannot do in integrated circuits if your goal is to make an integrated system.

8.6 Measurement Results

The input impedance of the fabricated cMUT devices are measured using a HP4195A Network Analyzer. Fig. 8.11 shows the real and imaginary parts of the membrane

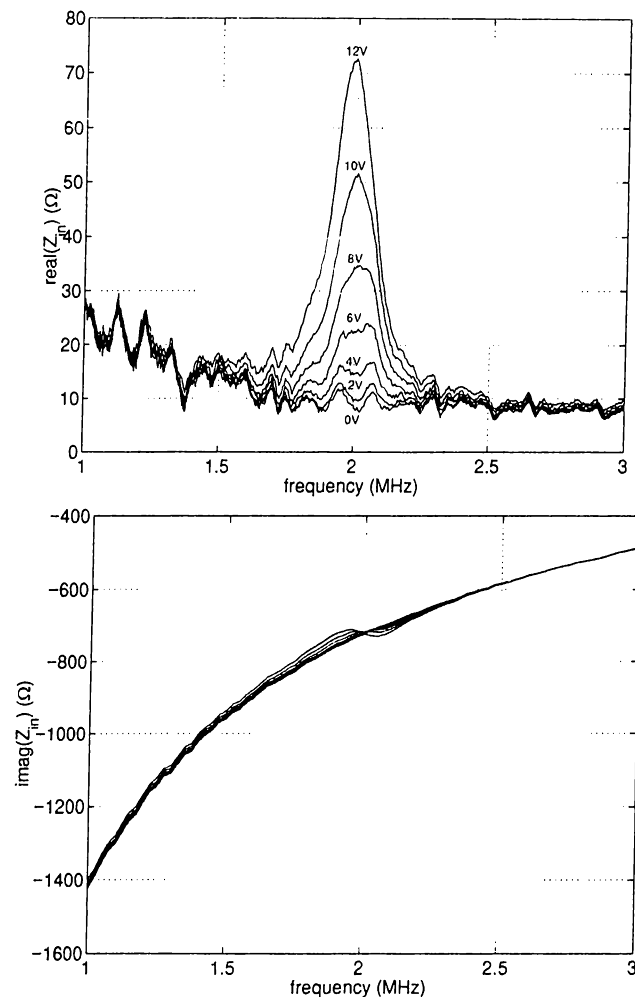

Figure 8.11: Real and imaginary parts of cMUT impedance for various bias voltages.

impedance as the bias voltage is changed. This behavior is predicted by the model circuit in Fig. 8.12. Without any bias, the electro-mechanical transformer of the model has zero transfer ratio, i.e., the effect of the acoustic port is not reflected to the electrical port. Hence, the frequency response that we see is that of a capacitor with a shunt ohmic loss. As the bias rises, the transformer ratio assumes a non-zero value, and this

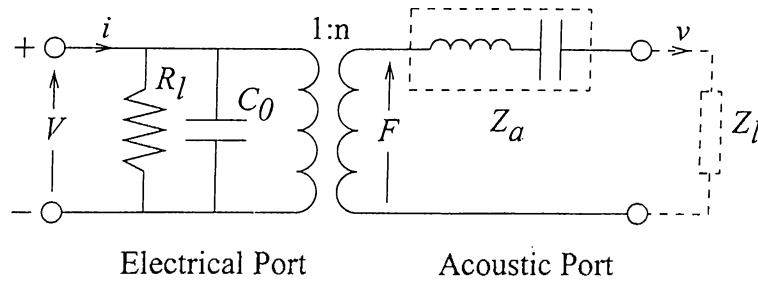

Figure 8.12: Simplified model for cMUT with ohmic losses.

is observed as the peak in the real part of the input impedance, and a slight twist in the imaginary part. Both of these occur at the mechanical resonance frequency of the membrane, which is at about 2 MHz for the particular device. The electrical input impedance

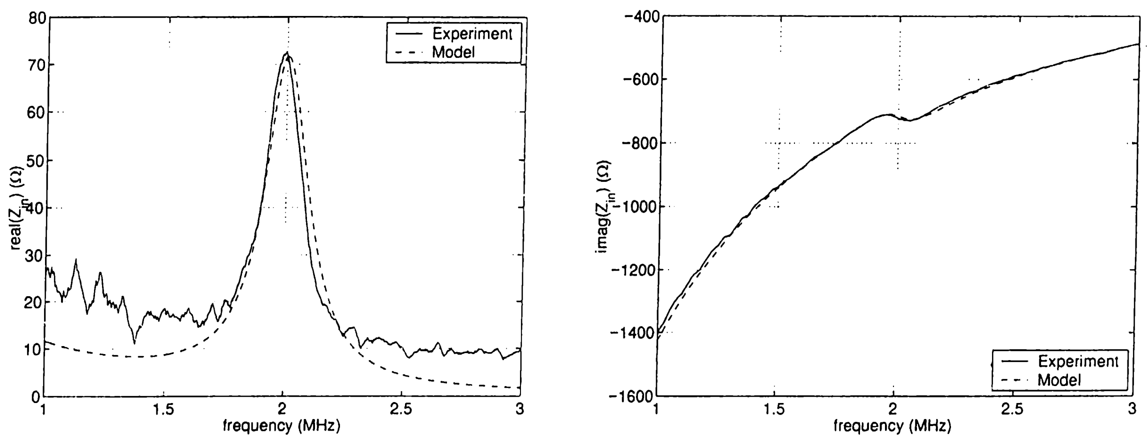

Figure 8.13: Experimental results and model data.

of the model circuit turn out to be consistent when compared to measurement data. By properly adjusting model parameters, the fit shown in Fig. 8.13 can be obtained.

Electrode Radius (μm)	Capacitance (pF)
8	72
16	86
24	110

Table 8.6: Shunt input capacitance of cMUT as a function of electrode radius.

Capacitance measurements for transducers of different electrode radii resulted in values listed in Table 8.6. An extrapolation of the data shows that the capacitances of

the interconnections and pads account for a value of about 67 pF, and the total value increased with increasing electrode area.

8.7 Discussion and Further Work

The material used for the membranes was low-temperature amorphous silicon which has finite resistivity. This accounts in the leakage term seen in the equivalent circuit representation. No measurement results were obtained from the detection experiment as all of the devices were shorted during experimentation. The possible cause is breakdowns occuring in the membrane material which is also used as an insulating layer between the bonding pads and the conducting substrate. The shorted device exhibits the electrical characteristics of two back-to-back diodes with reverse breakdown voltages at about 3 Volts. These are most probably the metal-semiconductor contact diodes formed by the silver epoxy GND connection and the gold electrode layer over the membrane material. There are two possible ways to solve this problem. First, the membrane material might be changed with some other silicon compound with higher resistivity. Second, an insulating substrate can be used. The latter requires the deposition of a ground electrode as the first step of the production process. The cost of an additional fabrication step can be compensated by the reduced input capacitance of the device, as none of the interconnections and bonding pads will be over ground planes, thus those will not contribute to the capacitance.

Another concern about the fabricated devices was about the holes etched for underetching the sacrificial layer. Those should be sealed if the device is to be used as an immersion transducer. As the development of a working air transducer took a considerably long time with quite low yield, the sealing step was not implemented, and the devices were tested only in air.

Chapter 9

CONCLUSION

The entire work on the modeling of Capacitive Micromachined Ultrasonic Transducers (cMUTs) yielded tools for the following analyses:

1. **Static Analysis** The behavior of the cMUT structure under the application of a DC bias voltage was analyzed. The shape of the membrane was determined for a small applied voltage for which the static electric field is assumed to remain unchanged with the changing shape of the membrane. The result of the small deflection problem was found to be consistent with existing theory. Being convinced about the accuracy of the FEM model, an iterative analysis was performed to determine the membrane shape when higher bias voltages were applied. This analysis revealed answers to questions like "what is the maximum bias voltage that can be applied without causing the membrane to collapse?" or "What is the DC capacitance of the deflected membrane?".

2. **Dynamic Analysis** cMUT dynamic parameters such as the acoustic impedance of the membrane and the electro-mechanical conversion efficiency were determined using a harmonic analysis. Again, results were justified with existing theory. The developed method was then employed in a optimization problem in which the best

top electrode size was determined. When bandwidth was chosen as the optimization criteria, the analysis result suggested an electrode which is as small as possible.

3. **Loss Analysis** The developed tools for the static and dynamic analyses were extended to handle an "infinite boundary value" problem. With the use of absorbing boundary conditions, an FEM model to analyze the behavior of a cMUT structure placed on a substrate of infinite radial dimensions was developed. This model was used to determine the effect of substrate loss to the electro-acoustic characteristics of the cMUT device. Normal mode theory was employed to give a better understanding of the nature of this loss mechanism.

All of the above mentioned tools can be used to design cMUT devices to meet certain design criteria, test the device characteristics prior to fabrication and predict the behavior of more complicated structures such as array transducers. As applications for the developed analysis tools, the electrode size for an immersion cMUT of radius 25 μm was optimized as bandwidth chosen as the optimization criteria. The optimum electrode radius was found to be 10 μm, using which the transducer bandwidth is almost doubled when compared to the fully metalized version. As a further study, the effect of substrate thickness on loss impedance was analyzed. Using the developed normal mode theory analysis, the dominant wave mode for a 500 μm thick silicon substrate was found to be the lowest order antisymmetric mode (A0).

Experimental results obtained from the fabricated devices support the basic model used in the whole study, but are yet insufficient to provide evidence for the correctness of the developed analysis tools. The fabricated cMUT devices are found to have a resonance frequency of 2 MHz. Due to problems resulting from the choice of the membrane material, detection experiments were not possible.

The analysis part can be further extended to include the loading effects of the surrounding medium. A 3-D model incorporating a load halfspace will even handle cross-coupling over the loading medium, which is suspected to be a significant source of cross-talk among array elements.

As described at the end of the experimentation part, further research directions for cMUT fabrication include the use of a insulating substrate for the fabrication of low input impedance transducers with increased electrical reliability. Finally, sealing the underetch holes will enable the cMUT devices to be used as immersion transducers.

Appendix A

A MICROMACHINING GLOSSARY

developer Chemical able to act on exposed photoresist. Exposed photoresist is "washed away" by the developer, which provides a mens to transfer the structure on the mask onto the structure.

directional etch Etch in which the etchant is unable to act evenly on the material. Directional etch can be achieved by either exploiting the crystal nature of the the material, or applying a mechanical etchant with particles moving in a certain direction (as in the case of reactive ion etch).

etch Removal of a material by either chemical or mechanical means. Micromachining basically relies on the selective nature of the etchant's corrosive effect on materials.

etchant Chemical or mechanical means used in etching.

exposure The application of uV light to photoresist. The presence of the mask between the light source and the sample coated with photoresist transfers the patterns on the mask onto the sample.

lithography Basic method used in carving the structures determined by the mask

onto the sample. Lithography starts with the coating of the sample with photoresist, continues with exposure and the application of the developer, and ends with etching.

mask A quartz plate on which the shape of the structures to be constructed in each step of the micromachining process are "drawn". The number of masks involved in the complete process determine the depth level of the fabrication.

plasma enhanced chemical vapor deposition Basic method involved in the deposition of materials onto the sample surface. The gases involved in the process determine which material is deposited, while the RF power used to create plasma, flow rate of gases and temperature affect the mechanical and chemical properties of the deposited layer. Done in a vacuum chamber.

photoresist A light sensitive "paint". The photoresist is the essential chemical involved in lithography. Known to be highly carcinogen.

reactive ion etch Mechanical etch in which the sample is placed under the bombardment of chemicals accelerated in RF plasma. While the used chemicals provide a selectivity, the direction in which the chemicals are accelerated determines the directivity of the etch. Done in a vacuum chamber.

selective etch Etch in which the etchant is inactive on the materials constituting the structure, but a single one. Selective etch is the most important tool used in the construction of micro-mechanical structures.

underetch A selective etch in which a material is removed from beneath another material. Underetch is the basic technique involved in the construction of suspended mechanical structures.

Appendix B

MATERIAL PARAMETERS

The following material praramteres have been used througout all simulations:

Material	E (kg/m·s^2)	ρ_{m0} (kg/m^3)	σ (unitless)	$\varepsilon/\varepsilon_0$ (unitless)
Air	1.00×10^{00}	1.29	0.499	1.00
Silicon Nitride	3.22×10^{11}	3270	0.260	7.50
Silicon Oxide	8.57×10^{10}	2651	0.075	3.90
Silicon	13.0×10^{10}	2332	0.278	11.8

E Young's Modulus

ρ_{m0} Mass Density

σ Poisson's Ratio

$\varepsilon/\varepsilon_0$ Relative Permittivity (Dielectric Constant)

Bibliography

[1] Khul, W., Schodder, G. R., and Schodder, F. K., "Condenser transmitters and microphones with solid dielectric for airborne ultrasonics," *Acustica*, vol. 4, pp. 520–532, 1954.

[2] K. Matzuwa, "Capacitive ultrasonic transducer," *J. Phys. Soc. Japan*, vol. 13, pp. 1533–43, 1958.

[3] Cantrell, John H. and Heyman, Joseph S., "Broadband electrostatic acoustic transducer for ultrasonic measurements in liquids," *Review of Scientific Instruments*, vol. 50, no. 1, pp. 31–33, January 1979.

[4] I. Ladabaum, X. C. Jin, H. T. Soh, A. Atalar, and B. T. Khuri-Yakub, "Surface micromachined capacitive ultrasonic transducers," *IEEE Trans. on Ultrasonics, Ferroelectrics and Frequency Control*, vol. 45, no. 3, pp. 678–690, May 1998.

[5] Soh, Hyongsok. T., Ladabaum, Igal, Atalar, Abdullah, Quate, Calvin F., and Khuri-Yakub, Butrus T., "Silicon micromachined ultrasonic immersion transducers," *Applied Physics Letters*, vol. 69, no. 24, pp. 3674-3676, December 1996.

[6] Ladabaum, Igal, Khuri-Yakub, Butrus T., and Spoliansky, Dimitri, "Micromachined ultrasonic transducers: 11.4 MHz transmission in air and more," *Applied Physics Letters*, vol. 68, no. 1, pp. 7–9, January 1996.

[7] Matthew I. Haller, *Micromachined Ultrasonic Devices and Materials*, Ph.D. thesis, Stanford University, 1997.

[8] Schindel, David W., Hutchins, David A., Zou, Lichun, and Say er, Michael, "The design and characterization of micromachined air-coupled capacitance transducers," *IEEE Transactions on Ultrasonics, Ferroelectrics, and Frequency Control*, vol. 42, no. 1, pp. 42–50, January 1995.

[9] P. Eccardt, K. Niederer, T. Scheiter, and C. Hierold, "Surface micromachined ultrasound transducers in CMOS technology," in *Ultrasonics Symposium*, San Antonio, Texas, November 1996, IEEE Ultrasonics, Ferroelectrics, and Frequency Control Society, pp. 959–962.

[10] Suzuki, K., Higuchi, K., and Tanigawa, H, "A silicon electrostatic ultrasonic transducer," *IEEE Transactions on Ultrasonics, Ferroelectrics, and Frequency Control*, vol. 36, no. 6, pp. 620–627, November 1989.

[11] Rafiq, M. and Wykes, C., "The performance of capacitive ultrasonic transducers using V-grooved backplates," *Measurement Science and Technology*, vol. 2, no. 2, pp. 168–174, February 1991.

[12] Pentti, Mattila, Tsuzuki, Fabio, Vaataja, Heli, and Sasaki, Ken, "Electroacoustic model for electrostatic ultrasonic transducers with V-grooved backplates," *IEEE Transactions on Ultrasonics, Ferroelectrics, and Frequency Control*, vol. 42, no. 1, pp. 1–7, January 1995.

[13] Anderson, Michael J., Hill, James A., Fortunko, Christopher M., Dogan, Numan S., and Moore, Russell D., "Broadband electrostatic transducers: Modeling and experiments," *Journal of the Acoustical Society of America*, vol. 97, no. 1, pp. 262–272, January 1995.

[14] Warren P. Mason, *Electromechanical Transducers and Wave Filters*, Van Nostrand, 1942.

[15] Prak, Albert, Elwenspoek, Miko, and Fluitman, Jan H., "Selective mode excitation and detection of micromachined resonators," in *Micro Electro Mechanical Systems Workshop*, Travemunde, Germany, 1992, IEEE Robotics and Automation Society, pp. 220–225.

[16] Voorthuyzen, J. A., Sprenkels, A. J., Van Der Onk, A. G. H., Scheeper, P. R., and Bergveld, P., "Optimization of capacitive microphone and pressure sensor performance by capacitor-electrode shaping," *Sensors and Actuators A (Physical)*, vol. 25-27, pp. 331–336, 1991.

[17] Gordon S. Kino, *Acoustic Waves: Devices, Imaging, and Analog Signal Processing*, Prentice-Hall, Inc., 1987.

[18] I. Ladabaum, X. C. Jin, H. T. Soh, A. Atalar, and B. T. Khuri-Yakub, "Surface micromachined capacitive ultrasonic transducers," *IEEE Trans. on Ultrasonics, Ferroelectrics and Frequency Control*, vol. 45, no. 3, pp. 678–690, May 1998.

[19] Ladabaum, I., Jin, X. C., Soh, H. T., Pierre, F., Atalar, A., and Khuri-Yakub, B. T., "Micromachined ultrasonic transducers: towards robust models and immersion devices," in *Ultrasonics Symposium*, Levy, M., Schneider, S. C., and McAvoy, B. R., Eds., San Antonio, USA, November 1996, IEEE Ultrasonics, Ferroelectrics, and Frequency Control Society, pp. 335–338.

[20] Jin, Xuecheng, Ladabaum, Igal, and Khuri-Yakub, Butrus T., "The microfabrication of capacitive ultrasonic transducers," in *Transducers 97*, Chicago, 1997, IEEE Electron Devices Society, pp. 437–440.

[21] Hohm, D. and Hess, G., "A subminiature condenser microphone with silicon-nitride membrane and silicon backplate," *Journal of the Acoustical Society of America*, vol. 85, no. 1, pp. 476–480, January 1989.

[22] ANSYS User Manual, *Volume I Procedures*, ©SAS IP, 1995.

[23] ANSYS User Manual, *Volume II Commands*, ©SAS IP, 1995.

[24] ANSYS User Manual, *Volume III Elements*, ©SAS IP, 1995.

[25] ANSYS User Manual, *Volume IV Theory*, ©SAS IP, 1995.

[26] Dale F. Ostergaard, "Adapting available finite element heat transfer problems to solve 2-d and 3-d electrostatic field problems," *Journal of Electrostatics*, vol. 19, pp. 151–164, 1987.

[27] R. Plonsey and R. E. Collin, *Principles and Applications of Electromagnetic Fields*, McGraw-Hill Book Company, Inc., New York, 1961.

[28] Tuttle,Jr. David F., *Electric Networks*, McGraw-Hill Book Company, 1965.

[29] R. M. Fano, "Theoretical limitations on the broadband matching of arbitrary impedances," *J. Franklin Inst.*, , no. 249, pp. 57–83, 139–154, January and February 1950.

[30] George L. Matthaei, *Microwave Filters, Impedance Matching Networks, and Coupling Structures*, Artech House, Dedham, MA, 1980.

[31] A. R. Levander, "Use of telegraphy equation to improve absorbing boundary efficiency for fourthorder acoustic wave finite difference schemes," *Bull. Seismil. Soc. Am.*, , no. 75, pp. 1847–1852, June 1985.

[32] C. Cerjan, D. Kosloff, R. Kosloff, and M. Reshef, "A nonreflecting boundary condition for discrete acoustic and elastic wave equations," *Geophysics*, , no. 50, pp. 705–708, April 1985.

[33] J. P. Berenger, "A perfectly matched layer for the absorption of electromagnetic waves," *J. Comput. Phys.*, , no. 114, pp. 185–200, 1994.

[34] W. C. Chew and Q. H. Liu, "Using perfectly matched layers for elastodynamics," in *IEEE Antennas Propagation Society International Symposium*. IEEE Antennas Propagation Society, 1996, pp. 366–369.

[35] F. D. Hastings, J. B. Schneider, and S. L. Broschat, "Application of the perfectly matched layer (PML) absorbing boundary condition to elastic wave propagation," *J. Acoust. Soc. Am.*, , no. 100, pp. 3061–3069, November 1996.

[36] Q. Liu and J. Ta0, "The perfectly matched layer for acoustic waves in absorbing media," *J. Acoust. Soc. Am.*, , no. 102, pp. 2072–2082, October 1997.

[37] X. Yuan, D. Borup, J. W. Wiskin, M. Berggren, R. Eidens, and S. Johnson, "Formulation and validation of berenger's PML absorbing boundary for the FDTF simulation of acoustic scattering," *IEEE Trans. on Ultrasonics, Ferroelectrics and Frequency Control*, , no. 44, pp. 816–822, July 1997.

[38] G. F. Miller and H. Pursey, "The field and radiation impedance of mechanical radiators on the free surface of a semi-infinite isotropic solid," *Proc. Royal Academy*, pp. 521–541, 1953.

[39] B. A. Auld, *Acoustic Fields and Waves in Solids*, Krieger Publishing Co., 1990.

[40] Bozkurt, A., Ladabaum, I., Atalar, A., and Khuri-Yalub B. T., "Theory and analysis of electrode size optimization for capacitive microfabricated ultrasonic transducers," *IEEE Transactions on Ultrasonics, Ferroelectrics, and Frequency Control*, vol. 46, no. 6, pp. 1364–1374, 1999.

[41] Haller, Matthew I.and Khuri-Yakub, Butrus T., "A surface micromachined electrostatic ultrasonic air transducer," in *Ultrasonics Symposium*, Cannes, France, 1994, IEEE Ultrasonics, Ferroelectrics, and Frequency Control Society, pp. 1241–1244.